Modeling and quantification of patterns of salinity, mixing and subtidal flow in estuaries, the role of river discharge and tidal forcing

A MPOC master thesis by:
Stavros Rafail Fostiropoulos

October 2, 2015

Supervised by:
prof. dr. H.E. de Swart
Wei Chen

.

Abstract

An estuary is a partially enclosed body of water along the coast where freshwater from river meets and mixes with salt water from the ocean. In this research study, significant aspects of estuarine physics, such as saltwater intrusion, stratification, vertical mixing and subtidal flow, are investigated. Obtaining more scientific knowledge about these physical processes occurring in estuarine regions, is essential for the preservation of natural environment and improvement of economic activity.

Specifically, it is investigated how saltwater intrusion, degree of stratification and vertical mixing depend on tidal forcing (S_2 tide) and river discharge is investigated, using a numerical model. Results are interpreted in terms of physical mechanisms that generate salt transport and subtidal flow. Further analysis is made regarding the subtidal flow generated inside the estuary by asymmetric mixing during the tidal cycle. The latter is represented by covariance between time-varying vertical mixing and vertical shear (CMS). Subtidal flow due to CMS is, in both cases investigated, up-estuary in the surface layer and down-estuary in the bottom layer. The most interesting result is that, subtidal flow is not only generated by CMS due to S_2 tide (tidal straining), but also by CMS due to S_4 tide.

.

Contents

.

1 Introduction

An estuary is defined by Cameron and Pritchard (1963) as a partly enclosed coastal body of water with one or more rivers flowing water into it and with a free communication with the open sea. Estuaries are areas which connect river and marine environments. One of the main physical processes that characterizes them is the mixing of saline ocean water and freshwater derived from land. An important source that provides for such mixing is the tidal current (Dyer, 1974). When the tidal current enters inside the estuary, it behaves as a tidal wave with decaying amplitude due to bottom friction. Freshwater entering in a coastal body of water generates longitudinal density gradients that result in long-term surface seaward motion and net landward motion underneath. This typical pattern of velocities is known as subtidal circulation. Pritchard was the first researcher to link the subtidal circulation to the forcing by the horizontal density gradient, using observations in the James River estuary which is located in the eastern United States. Subtidal circulation (Fig. 1) would be revealed if the vertically varying tidal currents are measured through a tidal cycle and then averaged. The typical strength of the subtidal currents ranges from $0.05\,\mathrm{ms}^{-1}$ to $0.3\,\mathrm{ms}^{-1}$, which is, approximately, an order of magnitude smaller than the strength of the tidal currents.

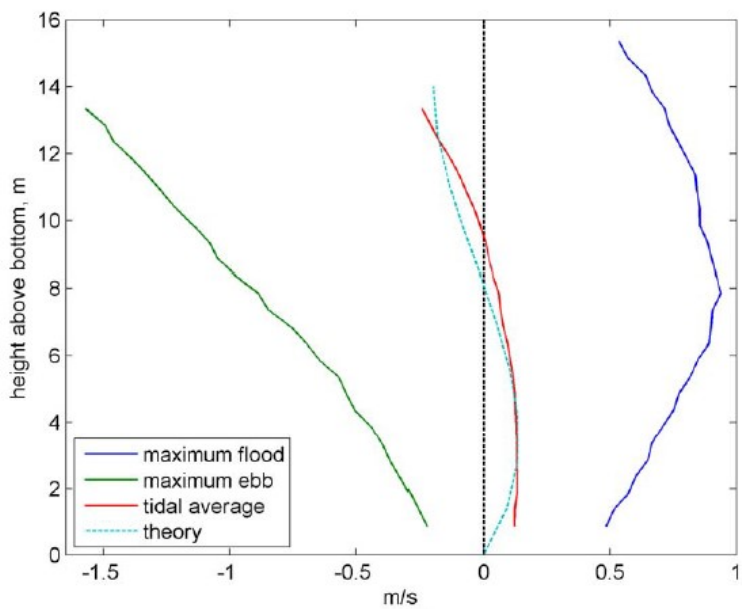

Figure 1: Vertical profiles of subtidal flow (solid red line), maximum flood tide (solid blue line) and maximum ebb tide (solid green line) obtained from observations. Vertical profile of theoretically predicted subtidal flow is indicated by dashed cyan line.

Competition between the tidal forcing and the freshwater input determines the strength of

the subtidal circulation, which in turns defines the water column stratification or salinity vertical structure inside the estuary. Among many different classifications of estuaries, one is in terms of vertical stratification. According to this type of classification, estuaries can be categorized as salt wedge, vertically mixed, strongly or weakly stratified (Fig. 2). As it was stated before, this classification considers the competition between buoyancy from river flow and mixing provided by tidal currents. Salt wedge estuaries result from strong river discharge and weak tidal forcing. Typical examples of salt wedge estuaries are the Mississippi (USA), Rio de la Plata (Argentina) and Ebro (Spain). Subtidal currents of these systems have strong seaward velocities throughout most of the water column and weak landward velocities close to the bottom.

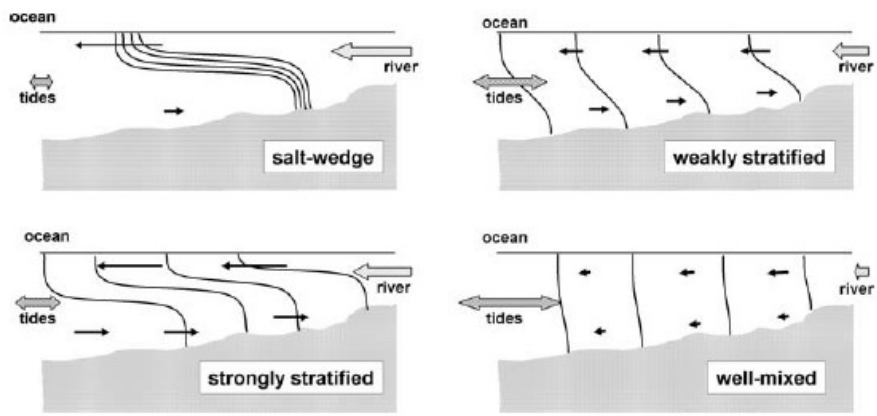

Figure 2: Classification of estuaries on the basis of vertical structure of salinity

Strongly stratified estuaries result from moderate to large river discharge and moderate tidal forcing. They experience strong stratification throughout the tidal cycle as in fjord and other deep estuarine systems. Mean flow in strongly stratified estuaries is characterized by weak inflow due to weak mixing with fresh water and weak horizontal density gradients. Weak to moderate river flow and moderate to strong tidal forcing result in weakly stratified estuaries. Their vertical salinity profile has continuous stratification from surface to bottom, except close to the bottom mixed layer. Weakly stratified estuaries have intense subtidal flow profiles, where inflow is strong enough because of the mixing between oceanic and fresh water. Estuaries such as Chesapeake Bay and Delaware Bay fit into this category. Finally, strong tidal forcing and weak river discharge result in vertically well mixed estuaries, where salinity profile is uniform and mean flow keeps the same direction with depth. In narrow well mixed estuaries, inflow of salinity may occur during the flood tide because the mean flow will be seaward, while in wide and shallow well mixed estuaries it is observed that inflows may occur on the one side across the estuary and outflows on the other side. An interesting remark is that estuaries may change classification with respect to the variability of the forcing agents that they are subjected to and the location inside the estuary. For instance, the Hudson River is classified as strongly stratified during the neap tide (weak tidal forcing), while during the spring tide (strong tidal forcing) it is classified as weakly stratified.

The motivation for the deeper understanding of estuarine physics is both of biological and economical relevance. Estuarine regions host a large amount of fauna. The dispersion of salt and nutrients due to the subtidal circulation is critical for the existence of these natural habitats. So from that point of view, physical investigation of estuaries is essential for the management of many factors regarding the preservation of these natural environments. Moreover, it has been found that zones of sediment accumulation at the bottom of the estuary are formed partly due to subtidal circulation (Postma, 1961; Talke et al., 2009). Since many estuaries host significant economical infrastructure like harbors and shipping routes which are sustained by sediment dredging, it is of great economical relevance to understand the physical mechanisms that accumulate sediment in those areas.

The first key problem that is investigated in this thesis concerns the saltwater intrusion which is the extension of salt water inside the estuary and it depends on the strength of tidal currents and river flow. Salt is imported inside the estuary due to spatial correlation between the subtidal flow and salinity and also due to horizontal diffusion of salt, while it is exported due to river flow. When the dominant mechanism that imports salt inside the estuary is the horizontal diffusion of salt, an analytical model by MacCready (2004) predicts that the dependence of saltwater intrusion distance L is inversely proportional to the river flow Q_r. On the other hand, when salt is imported mainly due to spatial correlation between the subtidal flow and salinity, the same model predicts that L is proportional to $Q_r^{-1/3}$. These theoretical expressions are applied to Delaware Estuary and North San Francisco Bay, and they show reasonable agreement with observations. The second key problem concerns the generation of subtidal flow by different driving mechanisms. Traditionally, the first drivers discovered that generate subtidal flow were the balance of horizontal salinity gradient with vertical mixing and the effect of river flow. The subtidal flow generated by theses mechanisms is usually referred as gravitational circulation (Pritchard, 1952, 1954, 1956; Hansen and Rattray, 1965). However, since then many different drivers that contribute to the generation of subtidal flow have been discovered. Simpson et al. (1990) pointed out a process that generates an asymmetry in stratification between ebb and flood. Due to bottom friction, the tidal currents are sheared towards the bottom, thus differential advection of horizontal buoyancy gradient occurs. During flood, the salt oceanic water is transported faster at the surface yielding reduced stratification (Fig. 3, upper panel), while during ebb less dense water is transported towards the surface and the stratification is enhanced (Fig. 3, lower panel). This mechanism is also known as tidal straining. How gravitational circulation and tidal straining generate subtidal flow, will be discussed in the next chapter. Of course there are other drivers, such as the Stokes transport pointed out by Jay (1991), which generate subtidal circulation but they are not considered in this thesis. Cheng et al. (2013) computed the subtidal flow generated by different drivers, and they focused on the contribution of asymmetric tidal mixing (ATM) to total subtidal flow for three different stratification regimes. Under periodically stratified conditions subtidal flow due to ATM is directed seawards at the upper half of the water column and in the opposite direction at the lower layer. At the weakly stratified regime subtidal flow due to ATM has a three-layer structure with landward flow near the surface and the bottom, and seaward flow in the middle of the water column. In highly stratified regime subtidal flow due to ATM is landward near the surface and seaward near the bottom. Note that in all three cases, tidal mixing is larger during flood than

ebb.

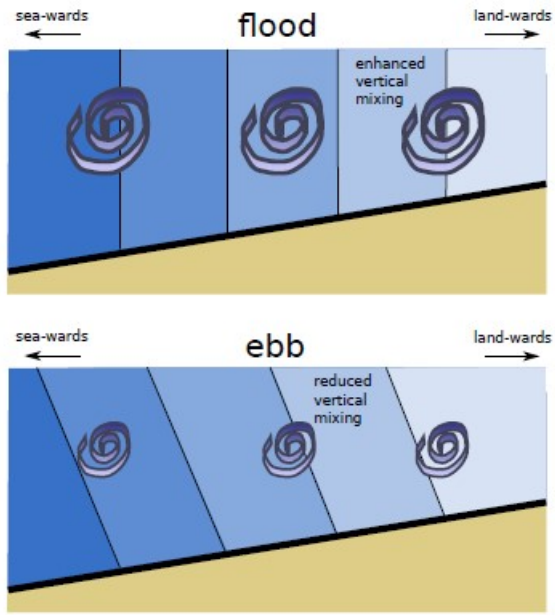

Figure 3: Sketch of the density distribution inside the estuary during flood (upper panel) and ebb (lower panel). The sea is to the left and the land to the right. Deep (light) blue colors indicate larger (smaller) density values. Large and small spirals stand for large vertical mixing (reduced stratification) and reduced vertical mixing (enhanced stratification), respectively.

The first aim of this study is to quantify the variation of saltwater intrusion and stratification under varying tidal current amplitude and river flow, and compare them with results from an analytical model (MacCready, 2004) and observations (Geyer, 2010; Monismith et al., 2002; Cheng et al., 2013). Regarding the second research question, subtidal flows generated from different drivers will be computed in the same way that Cheng et al. (2013) did. In this thesis, a case is considered, where tidal forcing and river discharge are both strong which is not investigated in Cheng et al. (2013) Under this regime subtidal flows provided by different drivers will be computed. Regarding asymmetric mixing, Cheng et al. (2013) found that the only responsible mechanism, in all three stratification regimes, that generates subtidal flow is tidal straining which is represented by the covariance of S_2 vertical eddy viscosity with S_2 vertical shear. In this thesis, covariance of vertical eddy viscosity with vertical shear (CMS) is decomposed into CMS due to S_2 and CMS due to S_4 in order to see if both of them can generate subtidal flow. A real time basin where the questions above can be addressed is the North Passage (NP) of Yangtze estuary in China. Yangtze estuary is subjected to strong seasonal variation in river flow with a monthly mean of $49.500\,\mathrm{m^2s^{-1}}$ during the wet season to $10.500\,\mathrm{m^2s^{-1}}$ during the dry season classifying it as one of the biggest rivers by discharge volume in the world. Furthermore, Yangtze estuary is subjected to varying tidal forcing, where the tidal elevation varies with a maximum of 4.5 m during the spring tide and a minimum of

2.5 m during neap tide. The length of North Passage is 60 km and the depth is 12.5 m after a Deep Waterway Project (Fig. 4) carried out from 1998 until 2011, while it's cross section is constant and equal to 4 km so to be considered as a narrow channel. Regarding the variability of tidal forcing and river discharge described before it should be clear that not all the amount of freshwater discharges inside the NP. Although from observations it is known that Yangtze river can discharge particularly inside the NP volume rates equal to $2400\,\mathrm{m^3s^{-1}}$. This value is much larger than the discharge rates used in the three regimes of Cheng et al. (2013). The research questions will be addressed by using a numerical model (Delft-3D), where an idealized model domain will be designed in a way to mimic the geometrical characteristics of North Passage. Tidal forcing and river discharge parameters will be set with respect to realistic parameters of NP in order the model to generate hydrodynamic conditions similar to that of NP.

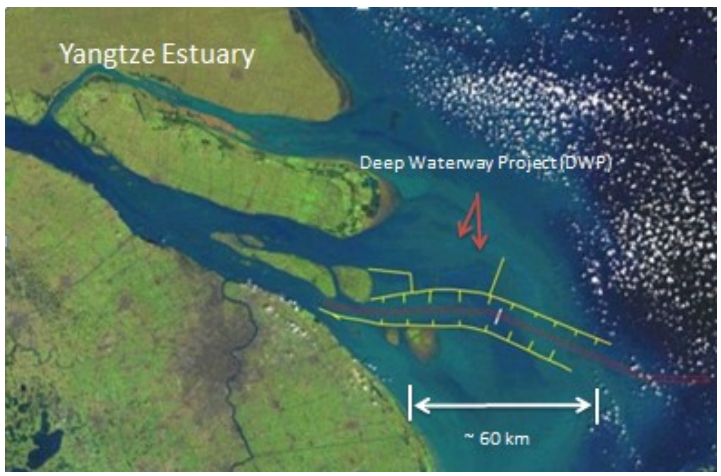

Figure 4: The Yangtze esturay. Yellow solid lines indicate the North Passage. Small lines vertical to North Passage show jetties which are an engineering construction of Deep Waterway Project (DWP)

The remainder of this thesis is structured as follows. In section 2, the theoretical concepts about gravitational circulation and asymmetric mixing are presented in detail. Moreover, the equations of the physical model, boundary conditions and the turbulence scheme are presented. Finally, the numerical domain and physical and numerical parameters are included, and methods that have been followed are described. In Section 3, results of the default about about tidal motion, subtidal flow, stratification and turbulent mixing are presented. Next, results of the sensitivity experiments are presented and specifically, penetration length, stratification and turbulent mixing for varying tidal forcing and river discharge. Moreover, contributions from different driving mechanisms to subtidal flow are quantified. In section 4, some remarks about dependence of stratification and saltwater intrusion on tidal current amplitude and river flow are discussed . Additionally, physical interpretation is given regarding the vertical structure of subtidal flow due to asymmetric mixing. Section 5 summarizes the main findings of the thesis.

2 Material and Methods

2.1 Theoretical concepts of subtidal flow in estuaries

2.1.1 Gravitational circulation

Gravitational circulation is defined as the the circulation generated by the horizontal density gradient and river run-off. The physics of this circulation was first discussed by Hansen and Rattray (1965). Fresh water from the river and salt water from the open sea, create a horizontal density gradient inside the estuary. This horizontal density gradient generates a baroclinic pressure gradient which drives the salt water of the bottom inside the estuary. The inflowing water raises the sea surface η near the head of the river, forcing surface water out of the estuary and rapidly enforcing the river flow (Fig. 5). These pressure gradient forces are balanced by frictional forces due to turbulent stresses. Due to mass balance, the sum of the volume flux of inflowing salt water and the river volume flux (Q_R) equals to the volume flux of the outflowing surface water (Q_1), thus $Q_1 = Q_2 + Q_r$. Typical velocity magnitude of gravitational circulation is $0.1\,\mathrm{ms}^{-1}$.

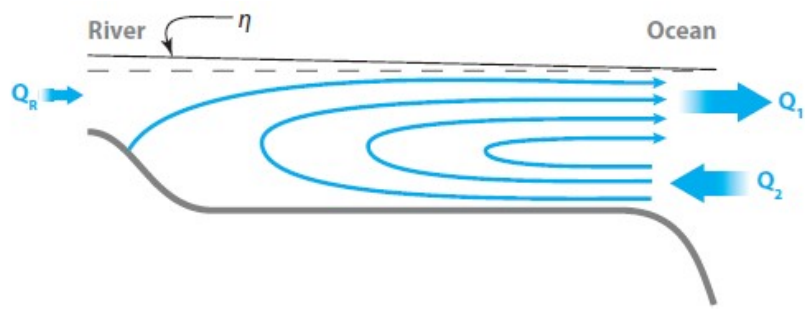

Figure 5: Tidally averaged circulation highlighting the graviational circulation with sea is at the right side and river is at the left. Derived from MacCready and Geyer (2009).

2.1.2 Subtidal flow due to Asymmetric tidal mixing (ATM)

Simpson et al. (1990) described how an asymmetry in density stratification between flood and ebb is generated. Due to bottom friction, tidal currents are sheared towards the bottom, and they induce a differential advection of the horizontal salinity gradient (Fig. 2). It has already been stated that this physical mechanism is known as tidal straining. One important consequence of tidal straining is its influence on the tidally averaged momentum balance and thus the subtidal flow. Jay & Musiak (1994, 1996) proposed that tidal variability of vertical mixing, which they referred to as tidal asymmetry, can contribute harmonics of the tidal frequency (M_4

component) and also enhance the gravitational circulation. Their observations at Columbia River showed that a strong M_4 shear flow is in phase with the flood tide near the bottom and out of phase with the ebb tide. They explained this by the increase of vertical mixing (reduced stratification) during flood and the suppression of vertical mixing (enhanced stratification) during ebb. Under this variation of stratification conditions during the tidal cycle, the covariance between eddy viscosity (K_z) and tidal shear ($\frac{\partial u}{\partial z}$) generates subtidal flow which is landward near the bottom and seaward near the surface (Fig. 6). Burchard and Baumert (1998) have found that magnitude of subtidal flow due to ATM can be up to factor 2 larger than the magnitude of subtidal flow driven by horizontal density gradient.

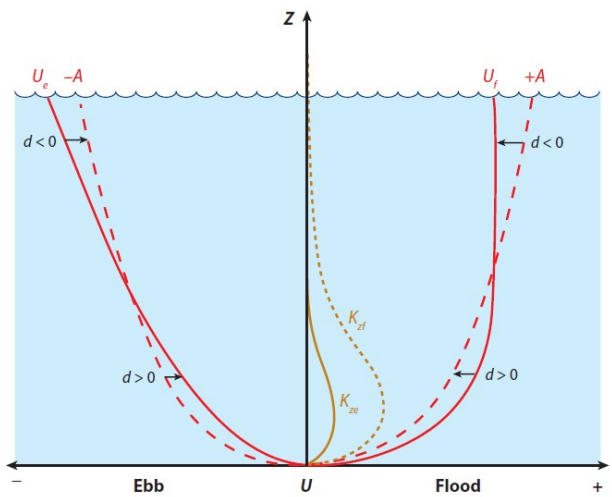

Figure 6: Ebb-flood asymmetry. Sea is at the left and river is at the right. Thick dashed lines $(-A, +A)$ indicate pure semi-diurnal tidal signal (symmetrical profile). Thick solid lines (U_f, U_b) indicate flood and ebb vertical velocity profiles. Signal of the asymmetry between the symmetrical profile and the actual profile is illustrated by d. Eddy viscosity profiles during flood and ebb are demonstrated by K_{zf} (thin dashed line) and K_{ze}(thin solid line), with stronger mixing occuring during the flood. Derived from Jay and Musiak (1994).

2.1.3 Subtidal flow due to other drivers

Other mechanism that generate subtidal flows, such as the Stokes drift and non linear advection, are discussed extensively in previous studies regarding the decomposition of residual currents (Ianniello, 1977; McCarthy, 1993).

2.2 Numerical model

Several numerical experiments were performed using the FLOW module of Delft3D modeling framework in order to simulate the hydrodynamic flow and the corresponding salinity field.

The DELFT3D-FLOW module solves the shallow water equations which consist of the hydrodynamic equations, the transport equation and a turbulence scheme. Delft3D-FLOW is ideal for simulating flows in estuaries as the vertical accelerations are neglected in the vertical momentum equation leading to hydrostatic pressure equation, which is realistic for shallow areas. For this study, in the horizontal and vertical direction, a Cartesian coordinates system and a σ-coordinate system have been chosen, respectively (Lesser et al., 2004).

2.2.1 The physical equations

In this subsection the equations of motion that constitute the basis of the model are discussed and their various terms are explained. The boundary conditions and the turbulence scheme, which is necessary to close the system, are also presented

Equation of state: In shallow water systems, temperature and pressure have negligible effect on density, so the latter depends only on salinity. Density does not vary much with respect to the average density, so a linear relationship holds:

$$\rho = \rho_*[1 + \beta(s - s_*)], \quad \beta = \frac{1}{\rho_*}\frac{\partial \rho}{\partial s}|_{s=s_*} \tag{1}$$

Here, ρ_* and s_* are the constant reference density and reference salinity respectively, while $\beta \approx 0.8$.

Continuity equation: Approximation of incompressibility of water in shallow areas is valid, so continuity equations reads

$$\vec{\nabla} \cdot \vec{u} = 0 \tag{2}$$

where, $\vec{u}$ is the velocity vector in three dimensions and $\vec{\nabla}$ is the nabla operator.

Salt balance: This yields the salinity equation

$$\frac{\partial}{\partial t}(\rho_* s) + \vec{\nabla} \cdot (\rho_* s \vec{u}) = 0 \tag{3}$$

The reference density ρ_* could have been canceled out from the equation, but retaining it allows for a better physical interpretation. For instance, the term $\rho_* s \vec{u}$ stands for the salt flux ($\mathrm{gm^{-2}s^{-1}}$). It should be stated here that this equation stands for motions on all feasible length and time scales. However, models usually can comprise only part of the spectrum of motions. For that reason, the variables are decomposed into a resolved part and an unresolved part, such as $\vec{u} =< \vec{u} > +\vec{u}''$. Here, the variable in between brackets represents the resolved part of the system and the variables with primes represents the unresolved part of the system. The brackets

stand for time and space averages over intervals that are large compared to the time scale and spatial scales of the unresolved motions, i.e. those of the turbulent motions. This implies that the averages of primed variables vanish. By decomposing the Eq. 3 into a mean and a turbulent part, it becomes

$$\frac{\partial}{\partial t}(\rho_* s) + \vec{\nabla} \cdot (\rho_* s \vec{u}) + \vec{\nabla} \cdot < \rho_* s'' \vec{u}'' >= 0 \tag{4}$$

Here, $\vec{\nabla} \cdot < \rho_* s'' \vec{u}'' >$ is the turbulent flux of salt which is parameterized as a linear function of the gradient of the average salinity and it is directed from regions of high salinity to regions of low salinity. This yields

$$< \rho_* s'' \vec{u}'' >= -\rho_* K_d \cdot \vec{\nabla} s \tag{5}$$

where K_d is a second-rank tensor and its components are turbulent diffusion coefficients of salt. Some remarks about the explicit relations of K_d will be given at the last part of the current subsubsection.

Momentum equations:

$$x: \quad \rho_*(\frac{du}{dt} + f_* w - f v) = -\frac{\partial p}{\partial x} + \frac{\partial \tau^{xx}}{\partial x} + \frac{\partial \tau^{xy}}{\partial y} + \frac{\partial \tau^{xz}}{\partial z} \tag{6}$$

$$y: \quad \rho_*(\frac{dv}{dt} + f u) = -\frac{\partial p}{\partial y} + \frac{\partial \tau^{xy}}{\partial x} + \frac{\partial \tau^{yy}}{\partial y} + \frac{\partial \tau^{yz}}{\partial z}$$

$$z: \quad \rho_*(\frac{dw}{dt} + f_* u) = -\frac{\partial p}{\partial z} - \rho g + \frac{\partial \tau^{xz}}{\partial x} + \frac{\partial \tau^{yz}}{\partial y} + \frac{\partial \tau^{zz}}{\partial z}$$

where the x, y, and z axes are directed eastward, northward, and upward, respectively, $f = 2\Omega \sin\varphi$ is the Coriolis parameter, $f_* = 2\Omega \cos\varphi$ is the reciprocal Coriolis parameter, p is the pressure, g is the gravitational acceleration, and the τ terms represent the normal and shear stresses due to friction.

Boundary conditions: In order the equations of motion to get solved, boundary conditions are required. A simple schematic is provided in Fig. 7 which shows where boundary conditions are applied. Here, $z = 0$ is the location of the undisturbed water level, $z = \zeta$ is the interface between water and air (also called the free surface), H is a constant reference depth and h is the elevation of the bottom with respect to $z = -H$.

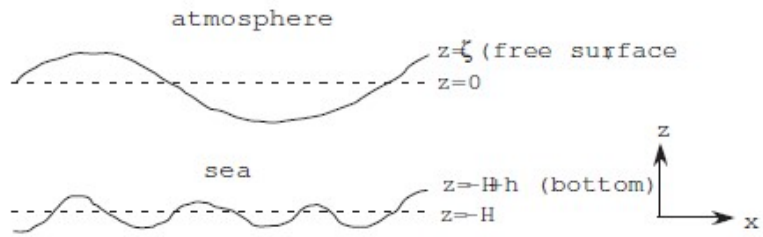

Figure 7: Schematic of a channel; side view. Derived from De Swart (2012).

Kinematic boundary conditions are applied at the bottom and the free surface, thus fluid elements can not escape. The relationships read

$$w = \frac{\partial \zeta}{\partial t} + u\frac{\partial \zeta}{\partial x} + v\frac{\partial \zeta}{\partial y} \qquad z = \zeta(x, y, t) \tag{7}$$

$$w = u\frac{\partial h}{\partial x} + v\frac{\partial h}{\partial y} \qquad z = -H + h(x, y) \tag{8}$$

Dynamic boundary conditions are also required, which impose continuity of the tangential stresses at the free surface of the sea.

$$p = p_0, \qquad \tau_{xz} \text{ and } \tau_{yz} \text{ continuous at } z = \zeta \tag{9}$$

where p_0 is the atmospheric pressure and τ_{xz} and τ_{yz} are shear stresses. Since the fluid is not ideal, an additional condition is imposed at the bottom. Velocity is represented by a logarithmic profile and it should vanish at a distance z_0 from the bottom. This results in a relation between the components τ_{xz} and τ_{yz} of vector $\vec{\tau_b}$ at this level and the horizontal velocity $\vec{u_b}$ at this level,

$$\overrightarrow{\tau_b} = \rho_* c_d |\overrightarrow{u_b}| \overrightarrow{u_b}\,, \qquad \text{at } z = -H + h \tag{10}$$

This relationship is known as the quadratic bottom stress law, where c_d is an empirical parameter called drag coefficient. Its value affects the profile of the horizontal velocity. In this study the Chezy formulation is selected for the computation of the bottom roughness profile. Furthermore, free slip conditions are imposed at the side walls.

The boundary conditions for salinity impose that there should be no transport of salt across any closed boundary ($G(x, y, z, t) = 0$). This implies that at any closed boundary the normal component of turbulent salt flux should vanish. This yields

$$(K_d \cdot \vec{\nabla} s) \cdot \vec{n} = 0 \qquad \text{at any closed boundary} \tag{11}$$

with $\vec{n} = \vec{\nabla} G / \left|\vec{\nabla} G\right|$.

Finally, at the open boundaries the water level, the normal velocity component or a combination should be prescribed to get a well-posed mathematical initial-boundary value problem. These data are obtained from measurements. Specifically, a semi-diurnal tidal elevation (S_2) is

imposed at the three open boundaries located at the open sea, while at the head of the estuary a river flow is specified (Fig. 8).

Turbulence scheme: After the decomposition of the instantaneous fluid motion to averaged flow and turbulent flow, the parametrization of the turbulent fluxes is necessary in order to close the system. The parametrization of turbulent salt flux in terms of a diffusion coefficient K_d has already been discussed. Regarding the turbulent fluxes of momentum, turbulent stresses τ_{ij} must be expressed in terms of state variables. A simple and often used closure scheme relates the turbulent shear stresses to velocity gradients and an eddy viscosity coefficient K (Pedlosdsky, 1978).

Here some remarks regarding the formulation of eddy viscosity and diffusion coefficients are provided. From now on eddy viscosity and eddy diffusivity will be indicated by A and K, respectively. Generalized formulation of the eddy viscosity and diffusion coefficient are of the type.

$$A_v = c_{\mu,v} U L \qquad K_v = c'_{\mu,v} U L$$

$$A_h = c_{\mu,h} U L \qquad K_h = c'_{\mu,h} U L$$

where U and L are characteristic velocity and length scales of turbulence, respectively, and $c_{\mu,v}$,$c_{\mu,h}$,$c'_{\mu,v}$, $c'_{\mu,h}$ are called stability functions. Stability functions, are functions of the gradient Richardson number Ri which reads

$$Ri = \frac{-\frac{g}{\rho_*}\frac{\partial \rho}{\partial z}}{\left|\frac{\partial \vec{u}}{\partial z}\right|^2} \tag{12}$$

The gradient Richardson number is the ratio of Brunt Vaisala frequency and the squared vertical shear of the flow. For $Ri > 0.25$ the water column is stably stratified and the turbulence is damped. The difficulty in formulating precisely the eddy viscosity and diffusivity coefficients lies at the fact that they depend on both space and time. For instance, when a tidal wave propagates inside an estuary with a rough bottom , the tidal wave generates turbulence with a characteristic velocity scale proportional to the local tidal flow amplitude. The tidal flow amplitude varies during the tidal cycle and for different locations, implying that the characteristic velocity scale U varies as well. In the same sense, typical turbulent length scale and stability functions vary with time and space. Among many turbulence schemes, the one that is used in this thesis is the $k-\varepsilon$ turbulence scheme which consists of two transport equations. The first equation is the turbulent kinetic energy notated by k, and the second one is the turbulent dissipation of energy notated by ε. After the two transport equations are solved for both turbulent kinetic energy k and turbulent dissipation ε, the mixing length L is then determined from ε and k according to

$$L_m = c_D \frac{k\sqrt{k}}{\varepsilon} \tag{13}$$

2.2.2 Model setup

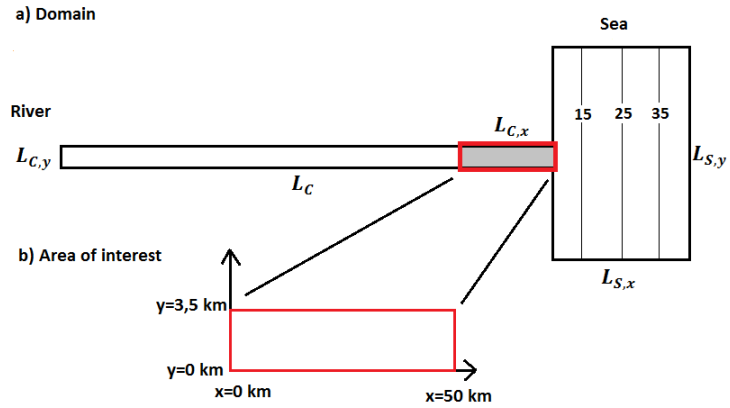

Figure 8: Schematic of the domain and bathymetry. For explanation of symbols see main text. Grey area (zoomed in) is the area of interest.

The model domain consists of a narrow and long estuary which is connected with an open sea. The sizes of the open sea and the channel are notated by $L_{S,x}$, $L_{S,y}$ and L_C, $L_{C,y}$ respectively, where x is the alongshore coordinate and y is the cross-shore coordinate. Inside the estuary, depth H_C is constant, while in the open sea depth is linearly increased from H_C to H_0. The shape of the model domain was selected in order to mimic the geometrical features of the study area (Fig. 8). The area of interest denoted by $L_{C,x}$ is a part of the estuary which starts at the connection between the estuary and the open sea and extends up to 50 km on-shore. Because of this, the results are presented for this specific area and not for the entire domain. The initial conditions for the water level η_0, salinity s_{oc} and temperature T_0 (Table. 1) are specified in the simulation. The model domain consists of four open boundaries, where at each one, flow and transport boundary conditions are prescribed. The value of salinity for the transport conditions ranges from 30 psu for the salt water to 0 psu for the fresh river water. Instead of drag coefficient c_d , a Chezy coefficient C is used which is related to c_d according to

$$c_d = \frac{g}{C^2} \tag{14}$$

Here, Chezy gets decreased from $65\,\mathrm{m}^{-\frac{1}{2}}\mathrm{s}$ to $30\,\mathrm{m}^{-\frac{1}{2}}\mathrm{s}$ as the tidal wave approaches the head of the river. The landward increase of friction is due to minimizing the chance for the wave to be reflected at the landward boundary and have an undesirable effect on the water motion inside the estuary. Finally, uniform background values for the vertical and horizontal viscosity and diffusivity have been set (Table. 1).

domain size	values
L_C	250 km
$L_{C,x}$	50 km
$L_{C,y}$	3, 5 km
$L_{S,x}$	50 km
$L_{S,y}$	50 km
H_C	10 m
H_0	40 m

Initial conditions	values
s_{oc}	30 psu
η_0	0 m
T_0	15 °C

Numerical parameters	values
K_h	$50\,\mathrm{m^2s^{-1}}$
K_v	$10^{-4}\,\mathrm{m^2s^{-1}}$
A_h	$50\,\mathrm{m^2s^{-1}}$
A_v	$10^{-4}\,\mathrm{m^2s^{-1}}$

Table 1: Size of the domain, initial conditions and physical parameters.

2.2.3 Numerical implementation

The model grid is 377 (along-channel) by 102 (cross-channel) by 10 (vertical direction) cells. The channel of the domain consists of 342 grid cells (250 km) along the channel and 7 grid cells across the channel (3.5 km). The grid size in the y direction is 500 m in the entire domain, while in the x direction the grid is refined locally from 2000 m (open sea) to 200 m (area of interest). A total of 10 vertical layers are distributed uniformly over the entire depth. The timestep should satisfy the Courant-Friedrichs-Lewy condition, and for this study it is selected as $\Delta t = 60$ sec. Simulation time varies with respect to the value of the river discharge. The amount of time needed for the fresh water to reach the mouth of the channel is calculated (Eq. 15) and a sufficient simulation time is set in order the model to reach steady state. This simulation time reads

$$t_{Sim.time} = \frac{L_C}{u_R} \tag{15}$$

In each case, the last two tidal cycles are used for the processing of the model output.

2.2.4 Design of experiments

Here, a matrix of the sensitivity experiments performed, is shown. A total of seven numerical experiments is performed including the default one. In three of the experiments the river flow is the default one and tidal forcing varies, and in the other three the tidal forcing is the default one and the river flow varies (Table. 2).

	$u_R\,(0.057\,\mathrm{ms^{-1}})$	$u_{R1}\,(0.051\,\mathrm{ms^{-1}})$	$u_{R2}\,(0.062\,\mathrm{ms^{-1}})$	$u_{R3}\,(0.068\,\mathrm{ms^{-1}})$
$\eta\,(1\,\mathrm{m})$	Default case	Small river flow	Medium river flow	Large river flow
$\eta_1\,(0.8\,\mathrm{m})$	Small amplitude			
$\eta_2\,(1.7\,\mathrm{m})$	Medium amplitude			
$\eta_3\,(2\,\mathrm{m})$	Large amplitude			

Table 2: Matrix of experiments. Rows and columns consist of values of river flow and tidal forcing (sea surface elevation), respectively.

2.3 Harmonic analysis

Harmonic analysis is a valuable mathematical tool as it is used for decomposing a signal in its dominant frequencies. In this study, harmonic analysis is applied extensively in time series of salinity, velocity and vertical mixing coefficients. Specifically, the physical quantities are decomposed to their mean and tidal part and the corresponding amplitudes are calculated. This is essential, as long as the subtidal circulation is under investigation. The general formulation of harmonic analysis for the velocity field reads

$$u = u_0 + \sum_{n=1}^{N} u_n \cos(n\omega t - \varphi_n) \tag{16}$$

where, the residual and the n-th velocity amplitudes are notated by u_0 and u_n respectively. Further, $\omega = 1,4 \times 10^{-4}\ s^{-1}$ is the radian frequency of the S_2 tide and φ_n is the phase of the n-th tidal harmonic. Salinity field is decomposed in the same way, and the formulation reads

$$S = S_0 + \sum_{n=1}^{N} S_n \cos(n\omega t - \theta_n) \tag{17}$$

where, S_0 accounts for the residual salinity profile, and S_n and θ_n account for the salinity amplitude and phase respectively, of the n-th tidal harmonic.

It has already been stated that the covariance between vertical eddy viscosity and vertical shear ($A_v \frac{\partial u}{\partial z}$) generates subtidal flow. In order to investigate if both CMS due to S_2 and CMS due to S_4 generate subtidal flow, harmonic decomposition of A_v is necessary and it reads

$$A_v = A_{v_0} + \sum_{n=1}^{N} A_{vn} \cos(n\omega t - \psi_n) \tag{18}$$

Here A_{v_0} and A_{vn} stand for the amplitude of residual eddy viscosity and the amplitude of n-th harmonic eddy viscosity, while ψ_n is the phase of n-th harmonic eddy viscosity. In case that asymmetric mixing occurs , the over-tide S_4 becomes stronger and the dominant amplitudes are A_{v_0}, A_{v1} (S_2-harmonic) and A_{v2} (S_4-harmonic). Having decomposed both vertical eddy viscosity and vertical shear (through decomposition of u), the term $A_v \frac{\partial u}{\partial z}$ can be decomposed as well. Note here that from now on A_{v1} and A_{v2} recast as A_{v,S_2} and A_{v,S_4}, respectively

2.4 Potential energy anomaly

A convenient way of evaluating processes of stratification and destratification, from a dynamical point of view, inside the estuary is the potential energy anomaly (Simpson, 1981). The latter is defined as the amount of mechanical energy per surface area required to homogenize the water column with a given density stratification and it reads

$$\Phi = -\int_{-1}^{0} H_C g \sigma \tilde{\rho}\, d\sigma \tag{19}$$

where, $\tilde{\rho}$ is the deviation from the depth average density, and g the gravitational acceleration. At this study a time-dependent equation of Φ, which is based on the dynamic equations for potential temperature and salinity, continuity equation and an equation of state for the potential density, is applied (Burchard and Hofmeister, 2008) and it reads

$$\partial_t \Phi = -\nabla_h(\bar{u}\Phi) + g\nabla_h\bar{\rho} \cdot \int_{-1}^{0} \sigma\tilde{u}\, d\sigma - g\int_{-1}^{0}(\eta - \frac{D}{2} - z)\sigma\tilde{u} \cdot \nabla_h\tilde{\rho}\, d\sigma - ...$$

$$... - g\int_{-1}^{0}(\eta - \frac{D}{2} - z)\sigma\tilde{w}\frac{\partial\tilde{\rho}}{\partial\sigma}\, d\sigma + g\int_{-1}^{0} K_v\partial_\sigma\rho\, d\sigma + g\int_{-1}^{0}(\eta - \frac{D}{2} - z)\sigma\nabla_h(K_h\nabla_h\rho)\, d\sigma \quad (20)$$

Here, $\bar{u}$ is the depth average velocity and $\tilde{u}$ is the deviation from the depth average velocity. The physical meaning of the first term on the right-hand side of the equation is the advection of Φ by the depth average horizontal velocity. The second term is the depth-mean straining, based on the vertical mean horizontal density gradient strained by the deviation from the depth-mean velocity vector. The third term is the non-mean straining, based on straining of the deviation from the vertical mean horizontal density gradient. The fourth term is the vertical advection which is based on the deviation from the linear vertical velocity. The fifth term represents the vertical mixing of density expressed as the integrated vertical buoyancy flux and the last term is the divergence of horizontal turbulent transport. Note that the unit of each term is Jm^{-2}.

2.5 Decomposition of total subtidal flow

Here, the total subtidal flow is decomposed into components generated by different driving mechanisms. These drivers have been presented in the beginning of this section. The total subtidal velocity reads

$$\bar{u} = \overline{u_R} + \overline{u_D} + \overline{u_{ATM}} + \overline{u_T} + \overline{u_S} \quad (21)$$

The subtidal flows generated are the river-induced flow ($\overline{u_R}$), the density driven flow ($\overline{u_D}$), the advection-induced flow ($\overline{u_A}$), the ATM-induced flow ($\overline{u_{ATM}}$) and the The Stokes return flow notated by ($\overline{u_S}$). Solutions of each subtidal flow are presented in Appendix. The aim of this analysis is to compute the contribution of each subtidal flow to total subtidal flow, but mainly to compare the these components under different stratification conditions.

3 Results

3.1 Default case

In this section the results of the default experiment are presented. In the first two parts velocity and salinity profiles are presented, and observations of stratification conditions are analyzed. Next, residual and tidal vertical eddy viscosity profiles at different locations of the estuary are shown. Furthermore, decomposition of vertical eddy viscosity into harmonic components is applied at two locations in order to investigate asymmetry in turbulent mixing. Finally, potential energy anomaly is applied to the last tidal cycle of the simulation in order to investigate how stratification varies, and the physical mechanisms that stratify and destratify the water column.

3.1.1 Velocity field

The tidal wave is generated in the outer sea and subsequently propagates into the estuary towards the head. The S_2 current amplitude is illustrated in the left panel of Fig. 9. It is clear that during the propagation of the tidal wave inside the estuary, the tidal wave's amplitude is decaying. The physical interpretation is as follows. Due to the presence of friction at the bottom of the channel, energy dissipation occurs which damps the tidal current amplitude as the tidal wave approaches the head. The damping depends also on the ratio of the tidal wavelength and estuary length. In this case the length of the estuary is large enough comparing to the tidal wavelength thus, the time that tidal wave will be subject to bottom friction is increased and as a consequence the decaying of the tidal current amplitude is enhanced. This evolution of tide inside the estuary refers to the characteristics of a traveling wave. Moreover, the bottom shear stress which represents the bottom friction is quadratic in the velocity (Eq. 10). This is justified from observations and dimensional arguments. According to the model result, the depth averaged tidal current amplitudes equal to $u_T = 0.75\,\mathrm{ms}^{-1}$ and $u_T = 0.5\,\mathrm{ms}^{-1}$ at the entrance (50 km) and the landward side (0 km) of the estuary, respectively. Right panel of Fig. 9 shows the phase of the tidal velocity. The phase increases in the horizontal direction showing how much time a trough of the tidal wave needs to travel from one location of the estuary to another. This increase confirms that tide behaves as a traveling wave. Finally, phase is almost the same in the vertical direction apart a small change close to the bottom due to friction. Besides the tidal wave, it's significant to see what happens by tidally averaging the velocity field. The periodic effect of the tide is filtered and the subtidal circulation u_0 is revealed. The two-layer flow in Fig. 10, is the characteristic pattern of subtidal circulation. Close to the bottom, subtidal velocities are directed up-estuary, and in the opposite direction at the layers close to the surface. The absolute values of the subtidal velocities become larger close to the mouth of the estuary. Note that the tidal velocity profile (Fig. 9, left panel) is an order of magnitude larger than the subtidal velocity profile (Fig. 10).

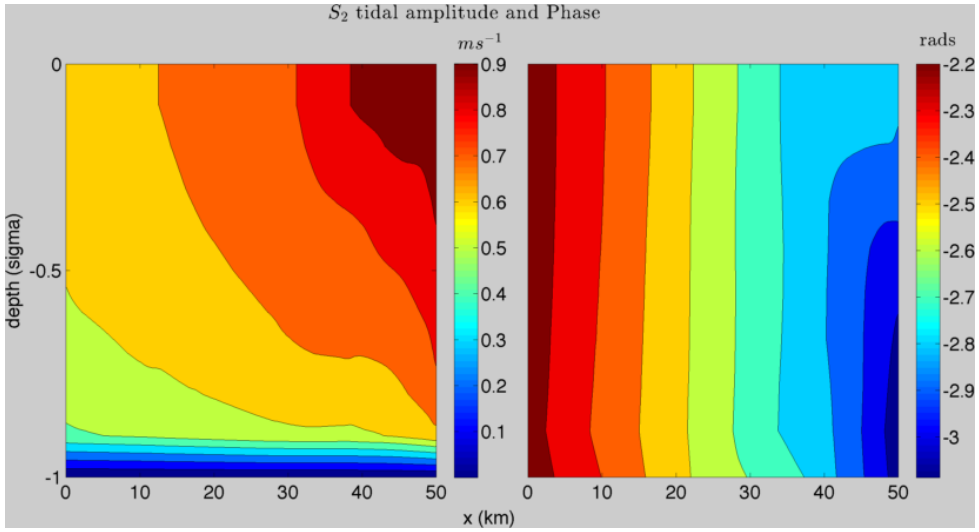

Figure 9: Amplitude (left panel) and phase (right panel) of S_2 tidal current versus distance x to river head and depth.

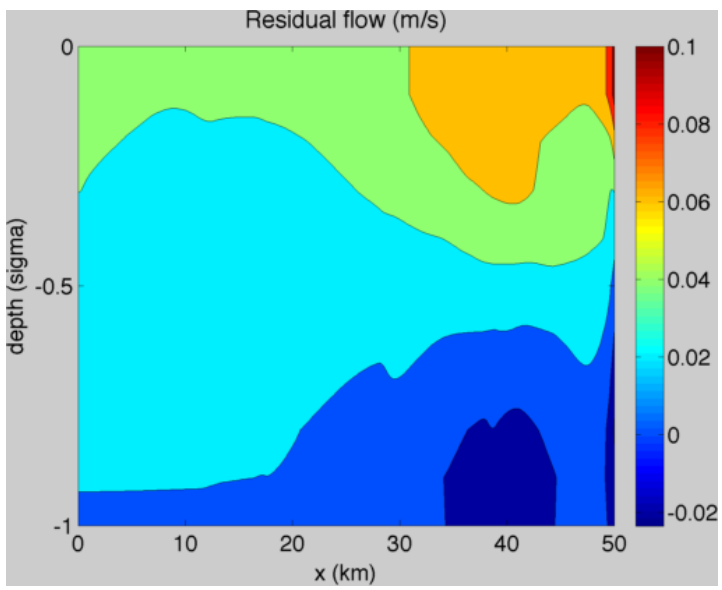

Figure 10: Subtidal velocity (colors, values in ms^{-1}) versus distance x to river head and depth.

3.1.2 Salinity-Stratification

Salinity is an essential aspect of estuarine dynamics. During flood, salt water is transported by the tidal flow inside the estuary where it interacts with fresh water and then ebb transports

the salt water to the open sea. The mechanism of import and export of salt is complex and it is explained in detail at the chapter 'Discussion'. Fig. 11 shows the variability of salt at the bottom of the estuary for the two last tidal cycles at $x = 30$ km and $x = 45$ km of the estuary. Peak in salinity occurs at the onset of ebb tide. The amplitude of salinity is larger at $x = 45$ km compared to $x = 30$ km, as this location is closer to the mouth.

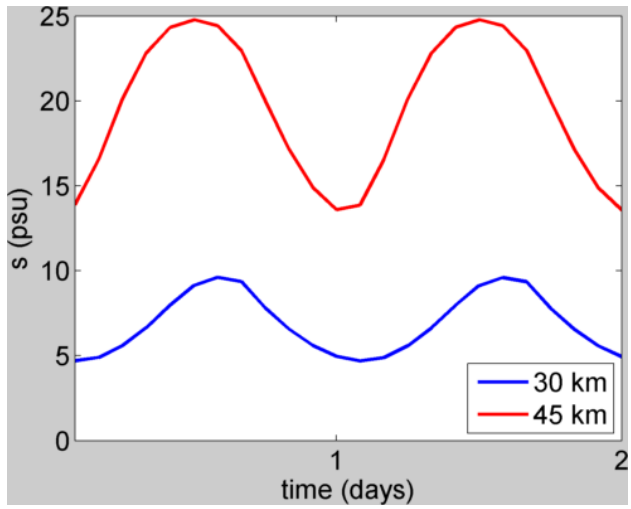

Figure 11: Bottom salinity during two tidal cycles at 30 km (blue line) and 45 km (red line).

The corresponding residual salinity profile indicates the amount of salt water intrusion and the mixing conditions inside the estuary. In Fig. 12, the subtidal salinity field (upper panel) and the degree of stratification (lower panel) are illustrated. The latter is computed by taking the difference between the salinity in the bottom layer and that in the surface layer. In the upper panel the level of saltwater intrusion, which is indicated by the white dashed line, is located at $x = 13$ km. The salt water limit is defined here as the location of the estuary where the tidally averaged salinity value at the bottom layer is equal to $s = 2$ psu. Regarding the vertical distribution of subtidal salinity, it is observed that in the first 35 km of the estuary, the isohalines are vertical to the along-channel direction which means that there is no deviation of salinity from it's depth-average value. This is also confirmed by the stratification diagram where top to bottom salinity difference is $\Delta s \simeq 0$ psu in the first 35 km of the estuary. This indicates that water is homogeneous in the vertical direction and consequently strong mixing occurs inside the water column. Inside the last 15 km from the mouth of the estuary, the effect of exchange flow slumps the isohalines at top and bottom to opposite directions. The consequent obliqueness of isohalines implies more salt water at the bottom layer than at the surface. Top to bottom salinity difference seems to increase linearly with a maximum of $\Delta s \simeq 2$ psu at the location of the mouth. Finally, a traditional classification based on stratification parameter at the mouth of the estuary is applied (Hansen and Rattray., 1956) The relationship reads.

$$\Phi_0 = \frac{\Delta s}{s_{oc}} \tag{22}$$

where Φ_0 is the stratification parameter, and s_{oc} is the salinity of ocean water. If $0 < \Phi_0 \leq 0.1$, the estuary is well mixed while for $0.1 < \Phi_0 < 1$ and for $\Phi_0 = 1$, it is partially mixed and highly stratified respectively. In this case, stratification parameter equals to $\Phi_0 \backsimeq 0.09$ so the estuary is characterized as partially to well mixed.

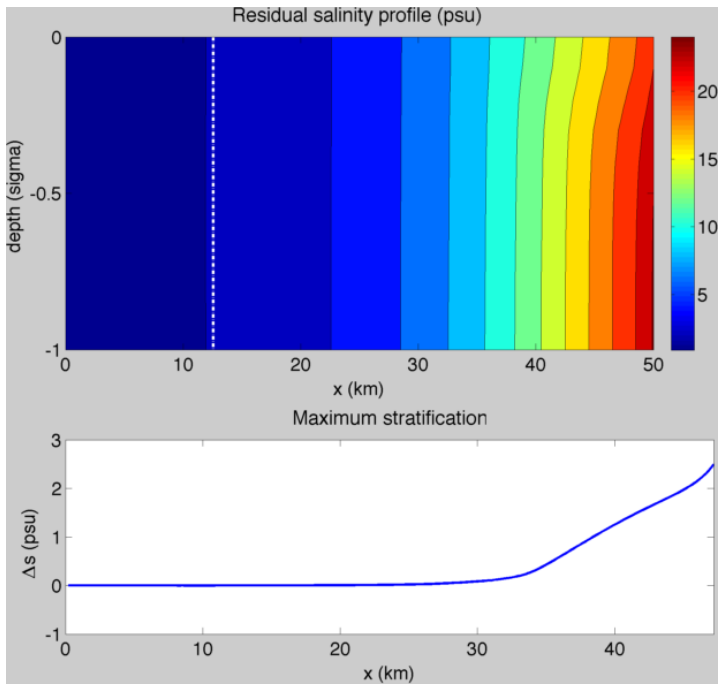

Figure 12: Upper panel: Residual salinity profile . Salinity difference (lower panel).

3.1.3 Turbelent Mixing

Turbulent mixing is generated by tides which propagate over a rough bottom, thus the magnitude of mixing depends on the magnitude of tidal forcing. The evolution of vertical eddy viscosity which expresses turbulent mixing is shown at two different locations inside the channel for the last tidal cycle of the simulation (Fig. 13). The locations have been chosen in such way to represent different stratification conditions inside the estuary. Vertical mixing, at the location $x = 30$ km (Fig. 13, upper panel), is strong during both the flood $(0 - 6$ hrs) and ebb phase $(6 - 12$ hrs). The strongest mixing is, as expected, at the peak of the ebb and flood tide, and it vanishes at the slack tide where there is no tidal motion. At 45 km inside the estuary, which is the location closest to the mouth, the characteristics of mixing differ from that at the location $x = 30$ km. The length over which turbulence intrudes into the water column but also its magnitude gets decreased during the flood phase (Fig. 13, lower panel). Indeed, a mixing asymmetry was expected at this location where tide is effective according to the theoretical

concept of asymmetric tidal mixing (ATM). Although the difference here is that turbulent mixing is larger during the ebb and not during the flood. Fig. 14 shows residual eddy viscosity profiles for different locations inside the estuary, where the mixing length is highlighted. From the salt water limit (3 km) up to 35 km, maximum of residual vertical eddy viscosity is at the middle of the depth with similar magnitudes ($A_{v_0} \backsimeq 0.18\,\mathrm{m^2s^{-1}}$), while for the rest 15 km the magnitudes are lower and the maximum vertical mixing occurs at 7 m. It is clear that turbulent mixing length decreases as the mouth of the estuary is approached . This result is in agreement with the stratification diagram of the previous subsection (Fig. 12, lower panel). Both vertical stratification and residual vertical eddy viscosity (Fig. 14) change their behavior at the same location ($x \simeq 34$ km) inside the estuary.

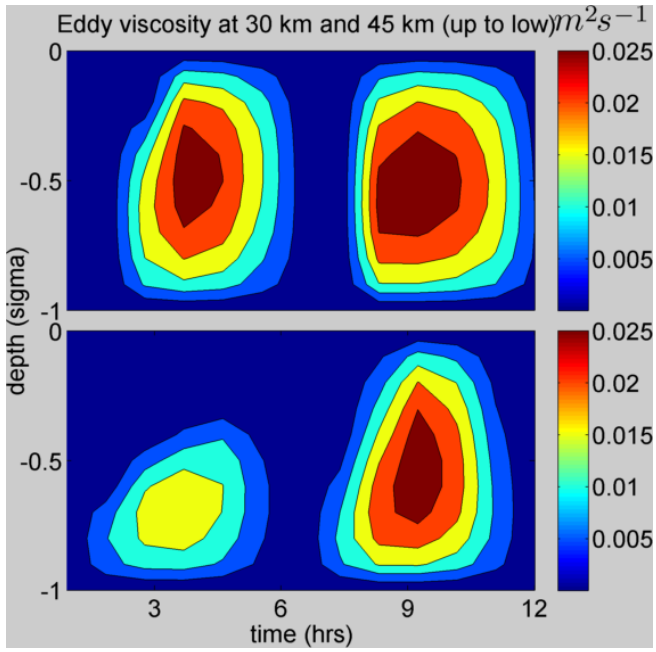

Figure 13: Vertical eddy viscosity during a tidal cycle at 30 km (upper panel) and 45 km (lower panel) inside the estuary. Flood tide occurs at $0-6$ hrs, while ebb tide occurs at $6-12$ hrs.

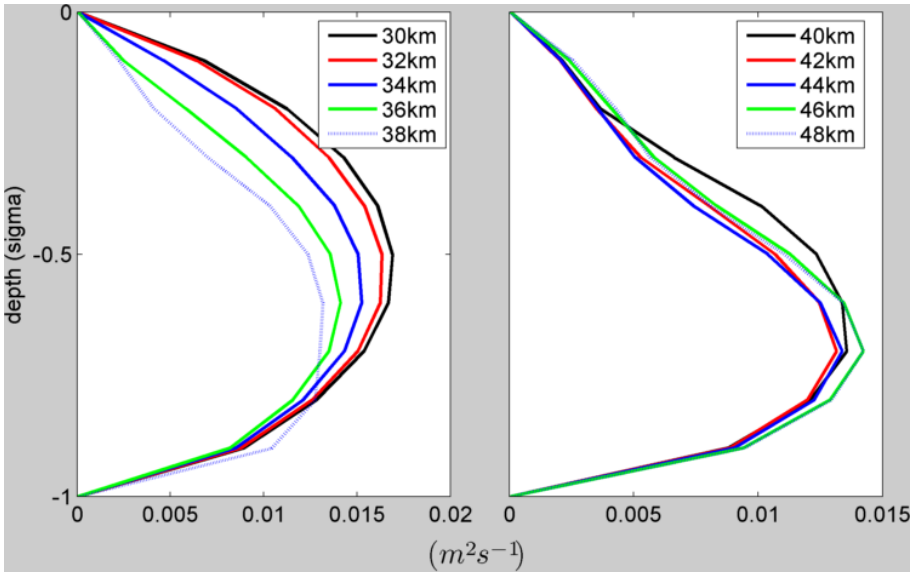

Figure 14: Residual eddy viscosity versus height. Different colors of solid lines indicate different locations inside the estuary.

A significant feature that should be discussed further is the ebb-flood mixing asymmetry which is observed at the vertical eddy viscosity during the tidal cycle (Fig. 13, lower panel). At the location $x = 30$ km which is remote from the mouth of the estuary it seems that there is no effect of S_2 tide at the production of vertical momentum flux. If someone computes vertical eddy viscosity at the middle of the depth for a tidal cycle, a time series will be found with two equal peaks at the maximum flood and ebb. The time difference between the two peaks is $t \simeq 6$ hrs, which yields an oscillation with quarter-diurnal signal. The most interesting case is at 45 km. At this location, the time series of vertical eddy viscosity has two unequal peaks which yield that two frequencies are dominant. This makes sense because at 45 km, tidal wave is not weak yet and it contributes at production of turbulent mixing. Decomposition of eddy viscosity field into harmonic components is essential for quantifying the contribution of each component in turbulent mixing. Fig. 15 shows A_{v_0} , A_{v,S_2} and A_{v,S_4} at 30 km and 45 km of the estuary.

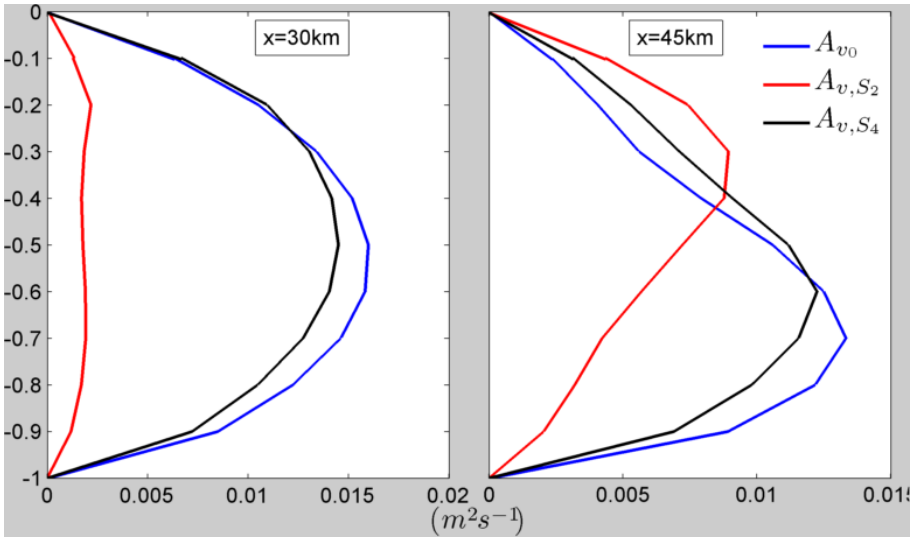

Figure 15: A_{v_0} (blue line) , A_{v,S_2} (red line) and A_{v,S_4} (green line) amplitudes at 30 km (left panel) and 45 km (right panel).

At 30 km, the contribution of S_2 tide to the vertical mixing is weak because a lot of energy dissipation has already occurred. Mixing is generated more due to subtidal flow and internal S_4 with maximum amplitudes at the middle of the water column equal to $A_{v_0} \simeq 0.015\,\mathrm{m^2s^{-1}}$, $A_{v,S_4} \simeq 0.014\,\mathrm{m^2s^{-1}}$. At 45 km (which is a location very close to the mouth) there is contribution from both S_2 and S_4 tide to vertical mixing as it was expected. A remarkable feature here is that S_2 amplitude is maximum close to the surface ($\sigma = -0.3$) and this is due to asymmetric mixing length between flood and ebb. The maximum amplitudes of eddy viscosity due to S_0, S_2 and S_4 tide are $A_{v_0} \simeq 0.014\,\mathrm{m^2s^{-1}}$, $A_{v,S_2} \simeq 0.008\,\mathrm{m^2s^{-1}}$ and $A_{v,S_4} \simeq 0.013\,\mathrm{m^2s^{-1}}$ respectively.

3.1.4 Potential energy anomaly

What has not been discussed yet is the fact that mixing is larger in ebb than in flood, which is in disagreement with previous model studies applied in similar domains (Cheng et al. 2013). This occurs because strong river discharge prevents turbulent mixing to homogenize the total water column during the flood phase. In Fig. 16 it is shown that, during the flood phase, turbulence starts mixing the water up to a certain depth of the water column. Specifically, a part of the water column which extents from the bottom up to $\sigma \simeq -0.3$ is well mixed, while at the rest of the water column the isohalines become oblique. It is observed also that the thickness of the turbulent boundary layer increases during the flood phase. However, due to strong river discharge, there is not sufficient time for the total water column to become well-mixed. The result is a two layer flow during the flood phase with stronger stratification comparing to the ebb phase. In order to understand this case where inverse turbulent mixing occurs, a dynamic equation for potential energy anomaly, as described in chapter 'Material and

Methods', is applied at the density field for the last tidal cycle at 45 km. It's significant also to understand how the terms from which the dynamic equation consists of, evolve with time. Upper and lower panel of Fig. 16 show the potential energy anomaly Φ and the balance of Φ-equation, respectively. Before the onset of ebb phase ($0 < t < 6$ hrs), fresh water is sheared over salty water and depth mean straining term (red solid line) starts increasing. Vertical mixing (black solid line) which balances the straining term decreases. Consequently potential energy anomaly increases. Before the stratification peak ($t = 3$ hrs), straining is reversed and supports now the vertical mixing which homogenizes the water column. Although the dominant mechanisms that build and collapse stratification are tidal straining and vertical mixing, there are also other mechanisms, such as Φ-advection (magenta solid line), which contribute in the balance of Φ-equation. The total contribution of these mechanisms ('plus sign' line) to balance of Φ-equation has a small deviation from the tendency (blue solid line), which is due to ignored terms in Φ-equation.

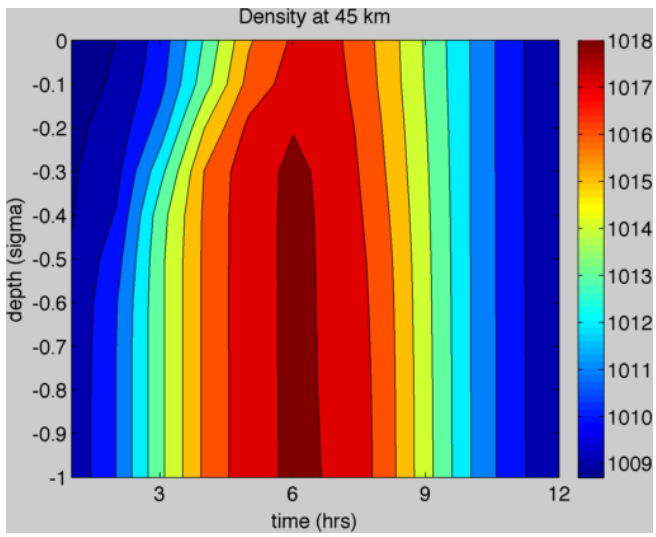

Figure 16: Time series of density field at 45 km. Flood tide occurs at $0 - 6$ hrs, while ebb tide occurs at $6 - 12$ hrs.

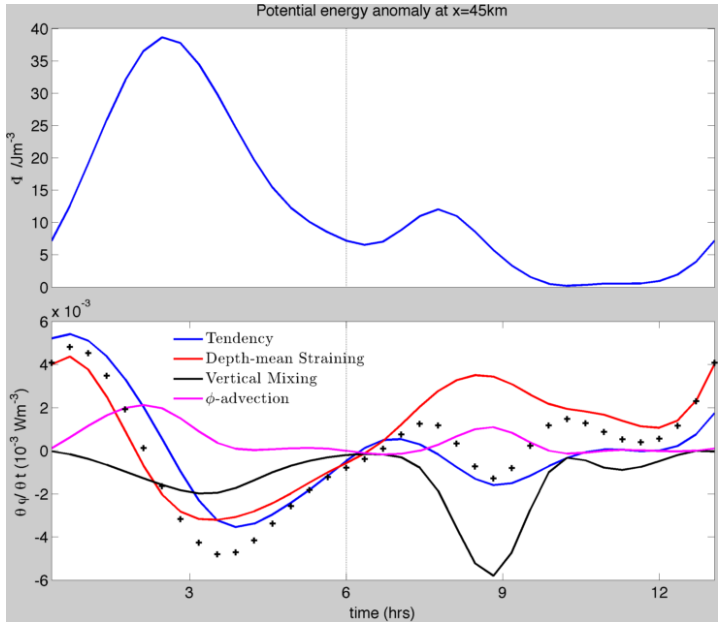

Figure 17: Upper panel; Time series of potential energy anomaly Φ. Lower panel: Time series of tendency $\partial_t \Phi$ (blue solid line), depth mean straining (red solid line), vertical mixing (black solid line) and Φ-advection (magenta solid line). 'Plus sign' line indicates the sum of depth mean straining, vertical mixing and Φ-advection.

3.2 Sensitivity analysis

Results of a number of sensitivity experiments are presented here. Firstly, the dependence of intrusion length and stratification on tidal current amplitude and river flow is considered. Next, the sensitivity of vertical mixing and subtidal circulation due to different drivers is determined for varying tidal current amplitude and the default river flow

3.2.1 Salt water intrusion

The salt water limit is defined here as the location where the salinity at the bottom layer is equal to $s_l = 2$ psu. Consequently, intrusion length L is the distance between the salt water limit and the mouth of the estuary. The extension of salt water towards the head of the channel depends on both tidal current amplitude and the magnitude of river flow. On the subtidal timescale, salt is imported into the estuary due to tides (import of saline water during flood, export of relatively fresh water during ebb) and due to horizontal turbulent diffusion. On the other hand, salt is transported out of the estuary due to the river flow. The left panel of Fig. 18 shows how intrusion length varies with tidal current amplitude at the mouth of the estuary. The river flow has its default value $u_R \simeq 0.057\,\mathrm{ms}^{-1}$. Intrusion length, for the experiment with the largest tidal current amplitude ($u_T \simeq 1.45\,\mathrm{ms}^{-1}$), is $L \simeq 41$ km which is the most extended

location of salt water inside the estuary. Salt water extends less towards the head of the estuary ($L = 36$ km) when tidal forcing is weak. Tidal current amplitude for this experiment equals to $u_T \simeq 0.8\,\mathrm{ms}^{-1}$. The right panel of Fig. 18 shows the variation of intrusion length with river flow. The tidal current amplitude has it's default value ($u_T \simeq 0.8\,\mathrm{ms}^{-1}$). The lowest river flow ($u_R = 0.051\,\mathrm{ms}^{-1}$) corresponds to intrusion length $L \simeq 44$ km, while the largest one corresponds to $L \simeq 31.5$ km. It is clear that when river flow increases, the intrusion length decreases.

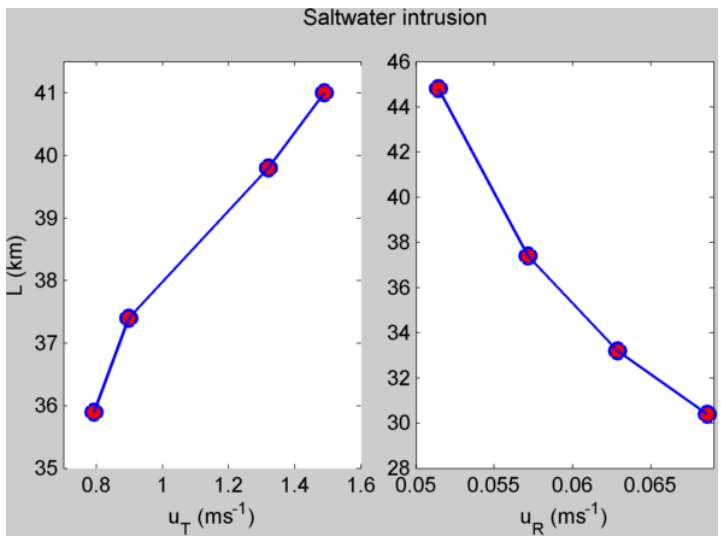

Figure 18: Saltwater intrusion versus tidal current amplitude (left panel) at the mouth of the estuary, and river flow (right panel). Other parameters have their default values (Table. 1).

3.2.2 Stratification and mixing

In this subsection, sensitivity of stratification to varying river flow and tidal current amplitude, is investigated at 45 km of the estuary. The motivation for choosing this location to evaluate stratification for different experiments is that this location is close to the mouth and there is significant variation of stratification for each experiment. At $x = 30$ km , which is a location remote enough from the mouth of the estuary, stratification is zero for all cases investigated. Left panel of Fig. 19 shows stratification, expressed as top to bottom salinity difference, versus tidal current amplitude at $x = 45$ km of the estuary (i.e., close to the mouth). The lowest tidal current amplitude ($u_T \simeq 0.63\,\mathrm{ms}^{-1}$) corresponds to the largest stratification equal to $\Delta s \simeq 6.5$ psu. It is found that stratification decreases with increasing tidal amplitude at 45 km. The right panel of Fig. 19 shows the dependence of stratification on river flow. The lowest river flow ($u_R = 0.051\,\mathrm{ms}^{-1}$) corresponds to the smallest stratification now ($\Delta s \simeq 1.2$ psu). It is clear that stratification increases with increasing river flow

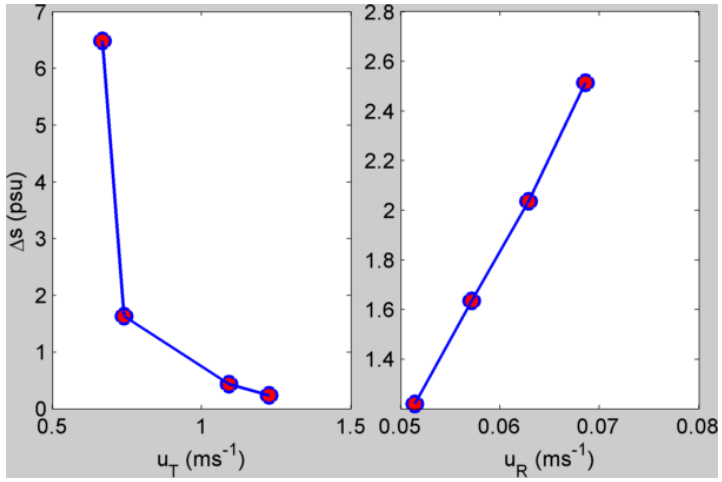

Figure 19: Stratification at location $x = 45\,\mathrm{km}$, expressed as top to bottom salinity difference, versus corresponding tidal amplitude (left panel) and river flow (right panel). Other parameters have their default values (Table. 1).

Another measure of stratification is the horizontal Richardson number which is the ratio of tidal energy to the stratifying effects of the baroclinic pressure gradient and tidal straining. Horizontal Richardson number indicates stratification and its relationship reads

$$Ri_x = \frac{\frac{g}{\rho_0}\frac{\partial \overline{\rho}}{\partial x} H_C^2}{c_d u_T^2} \tag{23}$$

Here, c_d is the bottom drag coefficient with a typical value of 0.0025. Note that horizontal Richardson number computed at a location where tidally averaged depth-mean salinity is half of that at the mouth of the estuary. Left panel of Fig. 20 shows that Ri_x decreases with increasing tidal amplitude, while it increases with increasing river flow (right panel).

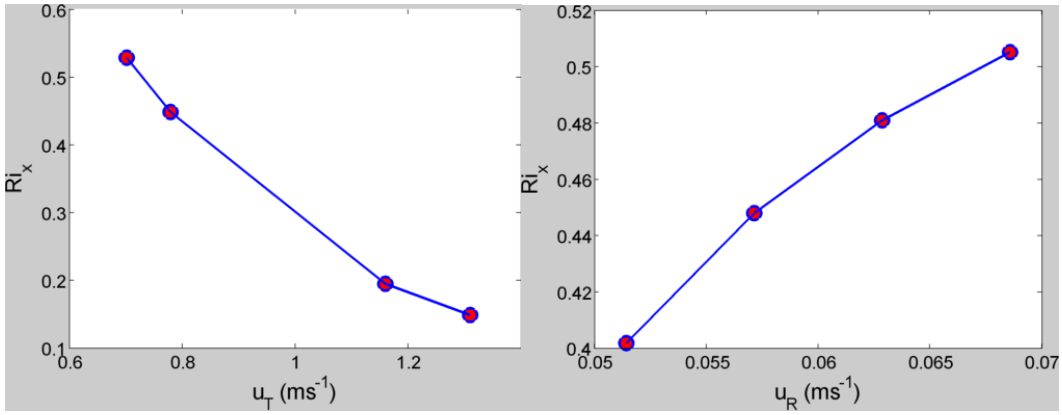

Figure 20: Horizontal Richardson number, at the location where the tidally averaged depth-mean salinity is half of that at the mouth, versus river flow and tidal amplitude at the estuary mouth. Other parameters have their default values (Table. 1).

Next, the effect of tidal forcing and stratification to vertical mixing is investigated. Residual profiles of vertical eddy viscosity indicate both the magnitude and the mixing length of turbulent mixing. Residual eddy viscosity is computed at 30 km (Fig. 21, left panel) and 45 km (Fig. 21, right panel). Moreover, A_{v,S_2} and A_{v,S_4} and the corresponding phase profiles are computed at 45 km.

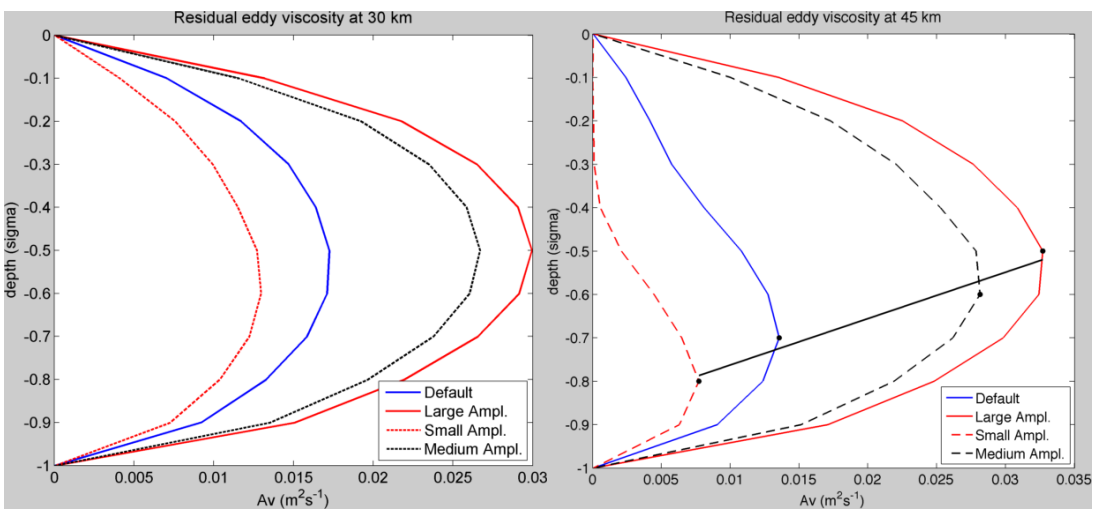

Figure 21: Vertical profiles of residual eddy viscosity for different tidal amplitudes, at 30 km (left panel) and 45 km (right panel) in the estuary. Black dots at right panel indicate the location of maximum eddy viscosity for each scenario. Tidal amplitudes are equal to $u_T \simeq 1.25\,\mathrm{ms}^{-1}$,$u_T \simeq 1.1\,\mathrm{ms}^{-1}$,$u_T \simeq 0.75\,\mathrm{ms}^{-1}$ and $u_T \simeq 0.63\,\mathrm{ms}^{-1}$ for the 'Large Amplitude', 'Medium Amplitude', 'Default Amplitude' and 'Small Amplitude', respectively. Other parameters have their default values (Table. 1).

In Fig. 21, the significant difference that is observed between the A_{v_0} profiles at 30 km and 45 km is the variation of turbulent mixing length . It seems that at 30 km mixing length remains constant for each different case and only the magnitude of maximum mixing decreases with tidal current amplitude. However at 45 km it is observed that not only the magnitude of maximum mixing but also the turbulent mixing length decreases with decreasing tidal current amplitude. Specifically, for the largest tidal amplitude, maximum mixing occurs in the middle of the water column with magnitude $A_{v_0} \simeq 0.033\,\mathrm{m^2s^{-1}}$. For the experiment with the lowest tidal amplitude, the magnitude of maximum residual eddy viscosity is decreased to $A_{v_0} \simeq 0,006\,\mathrm{m^2s^{-1}}$ and it occurs at $\sigma = -0.8$.

The vertical profiles of A_{v,S_2} and A_{v,S_4} and their corresponding phase are also computed at 45 km in the estuary. The maximum value of A_{v,S_2} (Fig. 22, Left upper panel) is smaller than that of A_{v,S_4}(Fig. 22, Left lower panel) for each experiment. Maximum value of A_{v,S_2} is located at $\sigma = -0.3$ for each experiment apart from the low amplitude experiment ($u_T \simeq 0.63\,\mathrm{ms^{-1}}$) where maximum value of A_{v,S_2} is located at $\sigma = -0.7$. Furthermore, it is clear the both maximum value and mixing length of A_{v,S_4} increases with tidal current amplitude

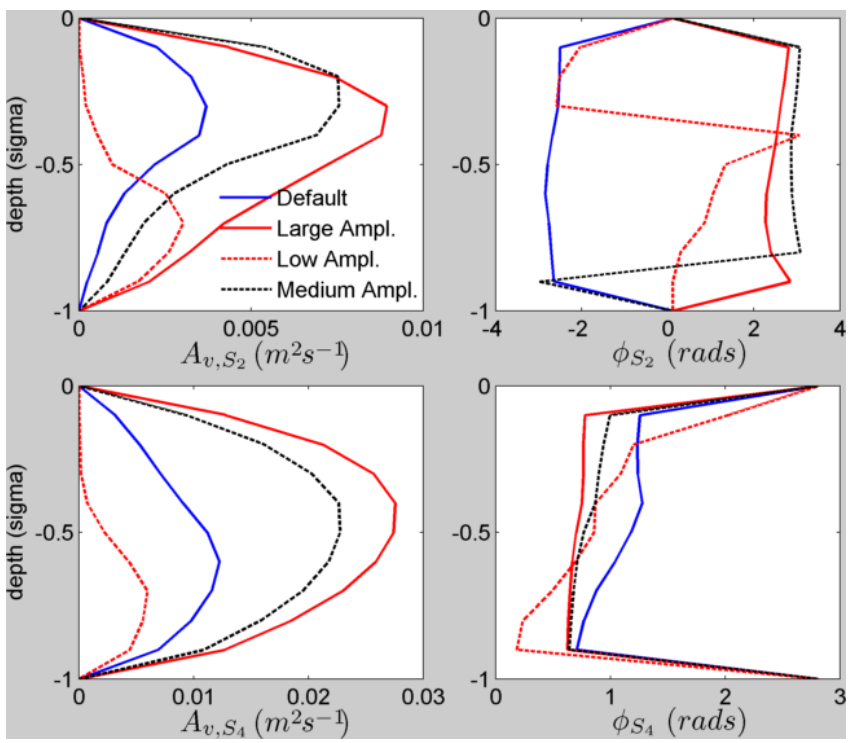

Figure 22: Vertical profiles of S_2 vertical eddy viscosity (Left upper panel) and phase (Right upper panel) and vertical profiles of S_4 vertical eddy viscosity (Left lower panel) and phase (Right lower panel) for the default experiment ($u_T \simeq 0.75\,\mathrm{ms^{-1}}$, solid blue line), the large amplitude experiment ($u_T \simeq 1.25\,\mathrm{ms^{-1}}$, solid red line), the medium amplitude experiment ($u_T \simeq 1.1\,\mathrm{ms^{-1}}$, dashed black line) and the low amplitude experiment ($u_T \simeq 0.63\,\mathrm{ms^{-1}}$, dashed red line). Other parameters have their default values (Table. 1).

3.2.3 Subtidal flow due to different drivers

Total subtidal velocity $\bar{u}$ is decomposed into subtidal flows generated by different forcing mechanisms. The contributors which are computed here are the river-induced flow ($\overline{u_R}$), the density-driven flow ($\overline{u_D}$) and the ATM-induced flow ($\overline{u_{ATM}}$). These components have been defined in chapter 'Material and Methods' and their analytical expressions are given in the Appendix. Subtidal flows, generated by nonlinear advection and Stokes transport, are not considered. This is because, the main aim here is to compare the behavior of ($\overline{u_R}$), ($\overline{u_D}$) and ($\overline{u_{ATM}}$) under different tidal forcing, rather than decompose in detail the subtidal flow to each single contributor. The terms ($\overline{u_R}$) and ($\overline{u_D}$) generate subtidal flow due to river run-off and horizontal density gradient, respectively. ATM-iduced flow ($\overline{u_{ATM}}$) is generated due to mixing asymmetries. Although, as it will be explained further in chapter 'Discussion', ATM-induced flow is not generated particularly due to asymmetric tidal mixing but more generally due to covariance between vertical mixing and vertical shear (CMS). However the notation 'ATM-induced flow' (Cheng et al., 2013) is kept. The contributors to total subtidal flow are computed for the default experiment ($u_T \simeq 0.75\,\mathrm{ms}^{-1}$) and for the case with the lowest tidal current amplitude ($u_T \simeq 0.63\,\mathrm{ms}^{-1}$) at 45 km of the estuary . Fig. 23 shows the vertical profiles of total subtidal flow $\bar{u}$ and the flow components ($\overline{u_R}$), ($\overline{u_D}$) and ($\overline{u_{ATM}}$) for the default experiment at 45 km of the estuary.

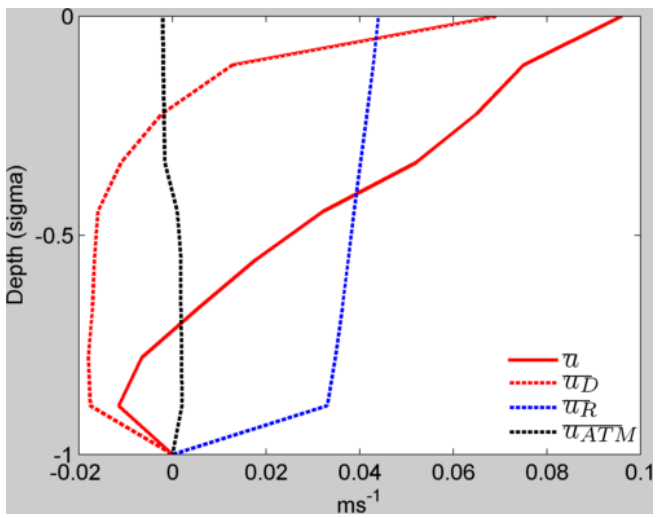

Figure 23: Vertical profiles of total subtidal flow $\bar{u}$ (solid red line), subtidal flow $\overline{u_R}$ due to river flow (dashed blue line), subtidal flow $\overline{u_D}$ due to density gradient (dashed red line) and subtidal flow $\overline{u_{ATM}}$ due to asymmetric mixing (dashed black line). The vertical profiles are computed for the default experiment ($u_T \simeq 0.75\,\mathrm{ms}^{-1}$) at location $x = 45$ km in the estuary. Positive (negative) velocities are down-estuary (up-estuary). Other parameters have their default values (Table. 1).

The river-induced flow is down-estuary ($\overline{u_R} \simeq 0.04\,\mathrm{ms}^{-1}$) and decreases from surface to bottom. The density-driven flow is directed up-estuary in the bottom layer up to $\sigma = -0.3$, while

in the upper layer, density-driven velocity is down-estuary. Maximum seaward and landward velocities are equal to $\overline{u_D} \simeq 0.07\,\mathrm{ms}^{-1}$ and $\overline{u_D} \simeq 0.018\,\mathrm{ms}^{-1}$ respectively. The subtidal flow $\overline{u_{ATM}}$ turns out to have the opposite structure of that of $\overline{u_D}$. It is down-estuary in the bottom layer and up-estuary in the surface layer. Note that in this case, ATM-induced flow does not contribute much to subtidal flow. Fig. 24 shows total subtidal flow $\bar{u}$ and the flow components ($\overline{u_R}$), ($\overline{u_D}$) and ($\overline{u_{ATM}}$) for the experiment with the lowest tidal current amplitude ($u_T \simeq 0.63\,\mathrm{ms}^{-1}$). The depth averaged value of $\overline{u_R}$ is equal to the one of the default experiment, as the river discharge is kept the same in both experiments. It turns out that if the tidal forcing is weak, river-induced flow shows more variation from surface to bottom than in the case of strong tidal forcing. Due to stratified conditions, mixing is weak in the upper layer compared to mixing in the lower layer. This causes the river-induced flow to be enhanced close to the surface and reduced close to the bottom. Density-driven flow is much stronger than that of the experiment in which tidal forcing is strong, as a result of weaker friction caused by smaller turbulent mixing. The up-estuary density-driven velocity equals $\overline{u_D} \simeq 0.1\,\mathrm{ms}^{-1}$ and it extends from the bottom up to $\sigma = -0.4$, while it becomes down-estuary close to the surface with maximum value at the surface equal to $\overline{u_D} \simeq 0.35\,\mathrm{ms}^{-1}$. The ATM-induced flow has a vertical structure that is opposite to the density driven flow, with a magnitude which is overall smaller than the latter. The physical interpretation regarding the vertical structures of $\overline{u_{ATM}}$ will be given in the next chapter. Finally, note the difference in scales between Figs. 23 and 24.

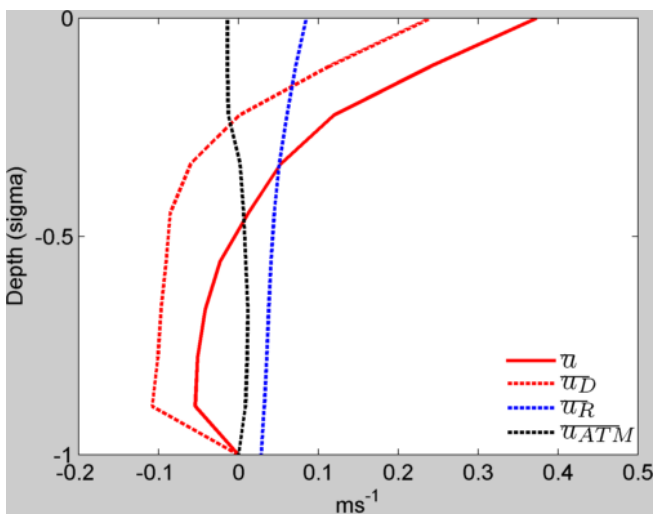

Figure 24: Vertical profiles of total subtidal flow $\bar{u}$ (solid red line), subtidal flow $\overline{u_R}$ due to river flow (dashed blue line), subtidal flow $\overline{u_D}$ due to density gradient (dashed red line) and subtidal flow $\overline{u_{ATM}}$ due to asymmetric mixing (dashed black line). The vertical profiles are computed for the experiment with the lowest tidal current amplitude ($u_T \simeq 0.63\,\mathrm{ms}^{-1}$) at location $x = 45$ km in the estuary. Positive (negative) velocities are down-estuary (up-estuary). Other parameters have their default values (Table. 1).

4 Discussion

4.1 Dependence of saltwater intrusion on tidal amplitude and river flow

Here, particular results from an analytical model by MacCready (2004) are used in order to interpret the dependence of saltwater intrusion on river flow and tidal current amplitude. The equations developed in this model consider only subtidal salinity and flow. The model computes the volume-integrated salt budget and the latter reads

$$\frac{1}{V}\frac{d}{dt}\int_R^x \overline{s}V dx = \overline{us} + \overline{u's'} - K_h\frac{d\overline{s}}{dx} \tag{24}$$

Here, $\overline{u}$ ($\overline{s}$) and u' (s') are the depth averaged and depth varying part of tidally-averaged velocity (salinity), respectively. The volume of water from a location $x = R$ inside the estuary, which is up-estuary in fresh water up to an arbitrary location x , is indicated by V. Finally, K_h is the along-channel diffusion coefficient. Note also that $\overline{u} = u_R$. The physical meaning of the l.h.s term of Eq. 24 is the salt storage which is zero for steady-state conditions. The first term on the r.h.s expresses the loss of salt due to river flow and the second and third term on the r.h.s express the import of salt due to exchange flow (gravitational circulation) and horizontal turbulent diffusion, respectively. In MacCready (2004) the solution technique showing the dependence of saltwater intrusion on river flow and tidal amplitude, is described explicitly. Under steady state conditions the salt budged is zero, and the salt balance is determined by the r.h.s terms of Eq. 24. In case that import of salt is dominated by exchange flow , the exchange limit is applied and the the turbulent diffusion term is ignored so Eq. 24 becomes

$$\overline{us} + \overline{u's'} = 0 \tag{25}$$

In the same way, the import of salt can be dominated by the turbulent diffusion, where exchange flow is ignored, and the diffusive limit is applied. In that case Eq. 24 becomes

$$\overline{us} + K_h\frac{d\overline{s}}{dx} = 0 \tag{26}$$

Under these simplifications, MacCready (2004) found that saltwater intrusion L varies as u_R^{-1} and $u_R^{-1/3}$ in the diffusive and exchange limit respectively. It is important to state that the variability of K_h can be important. For instance, Monismith et al. (2002), using salinity data from Northern San Francisco Bay, considered $K_h = 50\,\mathrm{m^2s^{-1}}$ and they found that saltwater intrusion is extremely insensitive to river flow ($u_R^{-1/7}$). They argued that this occurs because turbulent mixing is suppressed with increasing river flow, thus vertical eddy diffusion and viscosity get decreased. These in turn allow greater saltwater intrusion.

In order to see if the regime, in the default experiment, is exchange or diffusive dominated, r.h.s terms of Eq. 24 are computed according to Eq.2 from Diez-Minguito et al. (2013). The horizontal eddy diffusion K_h has its default value (Table. 1). Note that Diez-Minguito et al. (2013) do not assume balance and they consider also tidal pumping terms and Stokes transport which contribute as well to salt transport. Fig. 25 shows that the dominant mechanism that

imports salt inside the estuary is the horizontal turbulent diffusion indicated by black line and it is large enough compared to the import of salt due to exchange flow. The net salt transport, which is not shown in Fig. 25 is non zero when the export of salt by the river flow is added to the import of salt by exchange flow and horizontal turbulent diffusion. This is due to the fact that the contributions from tidal pumping terms and Stokes transport (turns out to be large) are not considered. Knowing now that the diffusive limit can be applied here, Eq. 26 (MacCready, 2004) is solved. The latter gives the relation between saltwater intrusion, river flow and tidal current amplitude, and it reads

$$L = \frac{K_h}{u_R} \tag{27}$$

In Eq. 27 it is clear that, in the diffusive dominated regime, L is inversely proportional to u_R. Furthermore, L is proportional to u_T in case that K_h is formulated in such a way to depend on u_T. From the results of Fig. 18 , which show the dependence of saltwater intrusion on river flow and tidal current amplitude in a diffusive dominated system, it is computed that L is proportional to $u_R^{-1.1}$ which shows larger sensitivity of L to u_R than the theoretically predicted. Regarding the dependence of saltwater intrusion on tidal current amplitude, they are independent between each other because K_h is set constant everywhere inside the estuary.

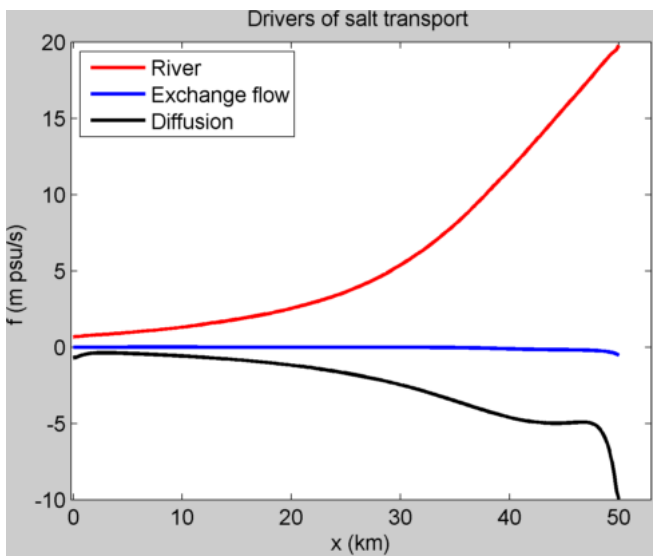

Figure 25: Contribution of physical mechanisms to salt transport. Export of salt is due to river flow (red line) and import of salt is due to horizntal turbulent diffusion (black line) and exchange flow (blue line)

4.2 Stratification

Values of top to bottom salinity difference indicate that tidal forcing which generates mixing consecutively dominates river discharge that creates buoyancy. For instance, value of top to

bottom salinity difference at the mouth of the estuary for the default configuration is equal to $\Delta s \approx 3$ psu. First remark that should be highlighted, regarding stratification, is the choice of horizontal diffusion parameter $K_h = 500\mathrm{m}^2\mathrm{s}^{-1}$ in the model. The initial option was to set a realistic horizontal diffusion $K_H = 50\,\mathrm{m}^2\mathrm{s}^{-1}$ but instability problems on salt transport appeared. Instability issues were solved by increasing K_h to $500\,\mathrm{m}^2\mathrm{s}^{-1}$ and set it constant everywhere inside the estuary. Consequently, all the numerical experiments in this thesis were performed with a non realistic horizontal diffusion. Later it was found out that instability issues can be solved by making a smoother grid, where the values of width and length will be the same at each 'grid box'. In order to avoid a time-consuming simulation with the new grid size, the model domain was decomposed into four sub-domains providing a more efficient computation. Horizontal diffusion was set equal to $K_h = 50\,\mathrm{m}^2\mathrm{s}^{-1}$ at the largest part of the estuary with exponential increase up to $K_H = 250\,\mathrm{m}^2\mathrm{s}^{-1}$ at the mouth, because there a lot of eddies are expected. Considering this realistic K_h and setting all the parameters equal to that of the default experiment, a new experiment was performed. It was found that top to bottom salinity difference equals to $\Delta s \simeq 11$ psu at 45 km in the estuary which is an order of magnitude larger than the top to bottom salinity difference ($\Delta s \simeq 1$ psu) in the default experiment.

For having a more clear estimation about the results of stratification, Δs and Ri_x are compared against observations (Geyer, 2010) and results from Cheng et al. (2013), respectively. Firstly, the river Froude number is computed through the relationship

$$Fr = \frac{u_R}{(g\beta s_{oc} H_C)^{1/2}} \tag{28}$$

for the experiments where the tidal amplitude has its default value ($u_T \simeq 0.75\,\mathrm{ms}^{-1}$) and the river flow varies. Here, β is the coefficient of isohaline contraction. Moreover, top to bottom salinity difference is scaled to oceanic salinity ($\Phi_0 = \frac{\Delta s}{s_{oc}}$). In Fig. 26 the black and white circles indicate Φ_0 and the corresponding Fr which have been observed in estuaries. The red circles indicate Φ_0 and corresponding Fr for the experiments, where the tidal amplitude has its default value ($u_T \simeq 0.75\,\mathrm{ms}^{-1}$) and the river flow varies. Note that Φ_0 has been computed at the mouth of the estuary in order to compare with observations. Regarding the results from the experiments, for values of river Froude number that range between $2 \cdot 10^{-2}$ and $3 \cdot 10^{-2}$, the corresponding Φ_0 ranges from $4 \cdot 10^{-2}$ to $8 \cdot 10^{-2}$. On the contrary, the observed Φ_0 , for the same interval of values of river Froude number, is larger than 10^{-1}. It's clear that Φ_0 resulted from the experiments is small compared to observations, implying that stratification in the experiments is underestimated.

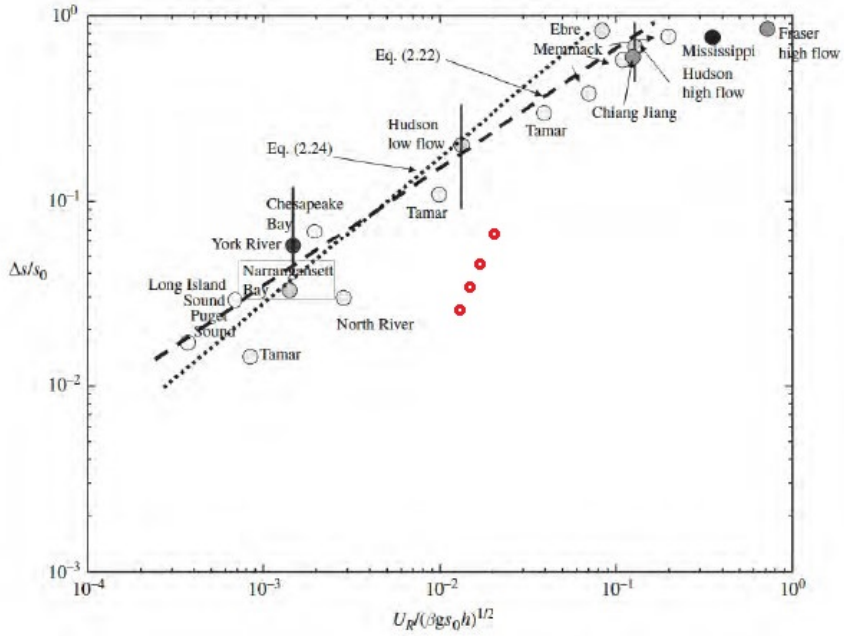

R

Figure 26: Scaled stratification Φ_0 versus river Froude number Fr . Dashed lines shows that Φ_0 is proportional to $Fr^{2/3}$ (this part of the sketch is inspired by Geyer (2010)). Red circles indicate Φ_0 versus Fr computed from the conducted experiments. Other parameters have their default values (Table. 1).

4.2.1 Horizontal Richardson number Ri_x

Here, the observed values of Ri_x (Fig. 27) from Cheng et al. (2013) are compared against the computed Ri_x for each experiment (Fig. 20). In Fig. 27 the river flow and the tidal current amplitude are indicated by u_f (cms^{-1}) and U_T (ms^{-1}) respectively. Note that the observed and computed values of Ri_x are compared against each other both for fixed river flow and varying tidal amplitude (horizontal red arrow) and fixed tidal amplitude and varying river flow (vertical red arrow). Fig. 27 shows that observed Ri_x decreases when tidal current amplitude increases (this behavior is not in agreement with the behavior of computed Ri_x). This is because these values of observed Ri_x stand for weakly stratified estuaries where Ri_x is inversely proportional to top to bottom salinity difference. Thus stronger tides lead to stronger stratification (Cheng et al., 2013). It is found that values of horizontal Richardson number from Cheng et al. (2013) are much larger ($Ri_x \simeq 1.5$) compared with the computed ones ($0.15 < Ri_x < 0.5$) which are shown also in left panel of Fig. 20.

Regarding the variation of horizontal Richardson number for fixed tidal amplitude and varying river flow, observed Ri_x increases with increasing u_f. Although that this increase is in agreement with the behavior of computed Ri_x (Fig. 20, right panel), the values of the latter are small enough compared with the observed Ri_x. It seems again that the reason for the underestimated computed Ri_x is that K_h is very large.

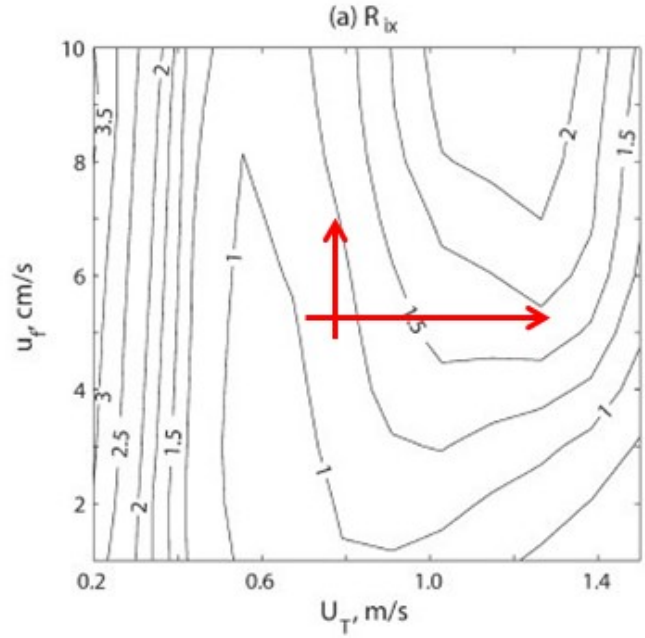

Figure 27: Horizontal Richardson number at location where the tidally averaged depth-mean salinity is half of that at the mouth, as a function of freshwater speed (u_f) and tidal current amplitude (U_T) at the estuary mouth (this part is derived from Cheng et al. (2013)). Red arrows in the u_f-U_T space indicate the observed Ri_x values which are compared with the computed Ri_x values.

4.3 Bottom boundary layer (h_{bbl})

The height of the bottom boundary layer (h_{bbl}) relative to the water depth in a stratified water column is given by Stacey and Ralston (2005). The relationship reads

$$\frac{h_{BBL}}{H_C} = (\frac{R_{fc}}{Ri_x})^{1/2}, \tag{29}$$

where R_{fc} is the critical flux Richardson number and is chosen as 0.2. The non dimensional height of bottom boundary layer is computed, for the experiments where tidal current amplitude varies and the river flow is fixed ($u_R = 0.057\,\mathrm{ms}^{-1}$), at a location where tidally averaged depth-mean salinity is half of that at the mouth of the estuary. From the results shown in Table. 3, it is clear that nondimensional height of bottom boundary layer increases with tidal current amplitude

$u_T\,(\mathrm{ms}^{-1})$	0.63	0.8	1.3	1.5
$\frac{h_{BBL}}{H_C}$	0.584	0.657	0.905	0.985

Table 3: Nondimensional height of bottom boundary layer (lower row) and the corresponding tidal amplitude (upper row) at location where tidally averaged depth-mean salinity is half of that at the mouth of the estuary. Other parameters have their default values (Table. 1).

4.4 Covariance of vertical eddy viscosity and tidal shear

Vertical distribution of ATM-induced flow is determined by the competition between two forcing mechanisms. This becomes evident by recasting Eq.40 in Appendix as

$$\overline{u_{ATM}} = \int_{-1}^{\sigma} \frac{1}{\overline{\overline{A_v}}} g \left(H_C^2 \frac{\partial \overline{\eta_{ATM}}}{\partial x} \sigma - \overline{\left[A_v' \frac{\partial u'}{\partial \sigma} \right]} \right) d\sigma \tag{30}$$

Here, the first component inside brackets in the r.h.s is the contribution that results from the barotropic pressure gradient. The second component reads

$$\overline{\left[A_v' \frac{\partial u'}{\partial \sigma} \right]} = \overline{A_v' \frac{\partial u'}{\partial \sigma}} - H_C^2 \left(\overline{\frac{2\eta}{H_C^3} \frac{\partial}{\partial \sigma''} \left(A_v \frac{\partial u'}{\partial \sigma} \right)} + \overline{\frac{2\eta}{H_C^3} \frac{\partial}{\partial \sigma} \left(A_v' \frac{\partial \bar{u}}{\partial \sigma} \right)} + \overline{\frac{2\eta}{H_C^3} \frac{\partial}{\partial \sigma} \left(A_v' \frac{\partial u'}{\partial \sigma} \right)} \right) \tag{31}$$

and stands for the mean stress that results from the covariance between time-varying vertical mixing and vertical shear (CMS). Note that the second term in the r.h.s of Eq. 31 is neglected because it is very small compared to the first r.h.s term, so the simplified mean stress becomes

$$\overline{\left[A_v' \frac{\partial u'}{\partial \sigma} \right]} = \overline{A_v' \frac{\partial u'}{\partial \sigma}} \tag{32}$$

Here the mean stress is decomposed into harmonic components in order to investigate contributions from 1) CMS due to S_2 tide and 2) CMS due to S_4 tide. Because of the ebb-flood mixing asymmetry, there is contribution to vertical mixing both from diurnal and semi-diurnal tide (Fig. 22, upper left panel and lower left panel). This results in a mean stress component that involves both covariance between A_{v,S_2} and $\frac{\partial u_{S_2}}{\partial \sigma}$ (tidal straining) and covariance between A_{v,S_4} and $\frac{\partial u_{S_4}}{\partial \sigma}$. The decomposition of the mean stress reads

$$\overline{A_v' \frac{\partial u'}{\partial \sigma}} = A_{v,S_2} \cos(\omega_{S_2} t - \varphi_{S_2}) \frac{\partial}{\partial \sigma} (u_{S_2} \cos(\omega_{S_2} t - \psi_{S_2})) +$$

$$+ A_{v,S_4} \cos(\omega_{S_4} t - \varphi_{S_4}) \frac{\partial}{\partial \sigma} (u_{S_4} \cos(\omega_{S_4} t - \psi_{S_4})) \tag{33}$$

Here, first term on the r.h.s is the S_2 mean stress component, where A_{v,S_2} is the S_2 harmonic component of vertical eddy viscosity with phase φ_{S_2}, ω_{S_2} is the S_2 frequency and u_{S_2} is the S_2 velocity amplitude with phase ψ_{S_2}. The second term is the S_4 mean stress component where A_{v,S_4} is the S_4 harmonic component of vertical eddy viscosity with phase φ_{S_4}, ω_{S_4} is the S_4 frequency and u_{S_4} is the S_4 velocity amplitude with phase ψ_{S_4}.

The S_2 and S_4 mean stresses are computed for the default experiment ($u_T = 0.8\,\mathrm{ms}^{-1}$) and for the experiment with the lowest tidal amplitude ($u_T = 0.63\,\mathrm{ms}^{-1}$) at location $x = 45$ km in the estuary. At this point it's important to highlight the vertical profiles of A_{v,S_2} and A_{v,S_4} (Fig. 22, upper left panel and lower left panel), for the default experiment (blue solid line) and the experiment with low tidal amplitude (red dashed line). At the default experiment, maximum A_{v,S_2} occurs close to the surface layer while maximum A_{v,S_4} occurs close to the bottom layer. On the contrary, at the experiment with the low tidal current amplitude both maximum A_{v,S_2} and A_{v,S_4} occur close to the bottom. This behavior is reflected at the vertical distribution of the S_2 and S_4 mean stresses and thus at the vertical distribution of the total mean stress. In Fig. 28, vertical profiles of S_2 (red solid line) and S_4 (blue solid line) mean stresses and the total mean stress (black solid line) are shown. Regarding the low tidal amplitude experiment (Fig. 28 right panel), where maximum mixing occurs during flood, both S_2 and S_4 mean stresses are negative and their maximum values are close to the bottom layer. Here it is clear that only the S_2 mean stress (red solid line) contributes to the total mean stress. This result is in agreement with Cheng et al. (2013), where under highly stratified conditions, tidal straining (only the covariance between A_{v,S_2} and $\frac{\partial u_{S_2}}{\partial \sigma}$) is the dominant mechanism for the generation of subtidal flow. Regarding the default experiment (Fig. 28 left panel), it's interesting that both S_2 and S_4 mean stresses contribute to subtidal flow and they have opposite signs. Note here that the maximum of S_2 mean stress occurs close to the surface where the maximum A_{v,S_2} is located as well (Fig. 22, upper left panel). The sign of S_2 mean stress is positive because maximum mixing occurs during ebb, thus the vertical shear is positive. The sign of the S_4 mean stress is negative and its maximum value is close to the middle of the entire column. In this experiment, it is evident that generation of subtidal flow occurs not only due to tidal straining (CMS due to S_2) but also due covariance of S_4 vertical eddy viscosity and S_4 vertical shear. The contribution from the two different profiles creates a total mean stress that switches sign with depth.

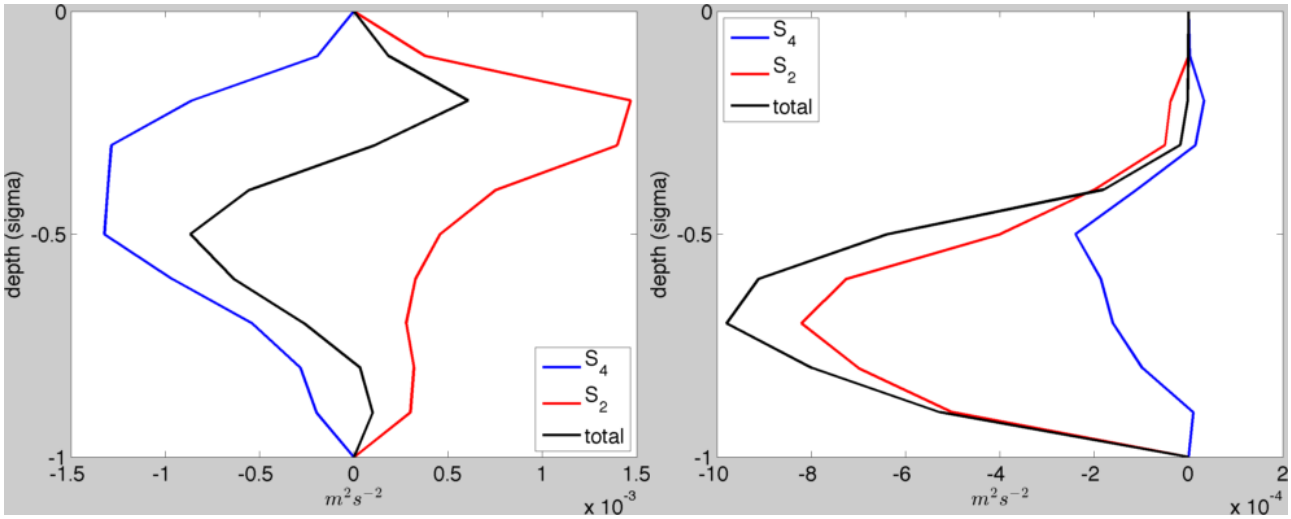

Figure 28: Vertical profiles of S_2 (solid red line), S_4 (solid blue line) and total (solid black line) mean stress for the default experiment ($u_T \simeq 0.75\,\mathrm{ms}^{-1}$) (left panel) and the experiment with low tidal amplitude ($u_T \simeq 0.63\,\mathrm{ms}^{-1}$) (right panel) at location $x = 45$ km in the estuary.

Now that the mean stress component of Eq. 33 has been decomposed and computed, the contribution from the barotropic pressure gradient (Eq. 30, first r.h.s term inside the brackets) is computed in order to investigate the subtidal flow generated due to CMS. At the experiment with the low tidal current amplitude, barotropic component is negative and it's magnitude is smaller than magnitude of mean stress close to the bottom layer and larger than that close to the surface layer. Consequently, the generated subtidal flow $\overline{u_{ATM}}$ is opposite to that of $\overline{u_D}$, with seaward flow close to the bottom and landward flow close to the surface. Similarly, $\overline{u_{ATM}}$ is computed for the default experiement and it is found to be up-estuary in the upper layer and down-estuary in the lower layer.

4.5 Suggestions for future research

As a future suggestion it would be valuable to perform again all the numerical experiments by designing a smoother grid, as suggested in subsection 4.2, in order to avoid the instability problems for small values of K_h. This allows to set a realistic horizontal eddy diffusion coefficient $K_h = 50\,\mathrm{m}^2\mathrm{s}^{-1}$ which is constant in most of the domain and it increases exponentially close to the mouth because a lot of eddies are expected. A significant aspect of estuarine hydrodynamics which has not been discussed in this thesis is the lateral flow. Despite the fact that the simulations were performed for a 3-D model domain, the lateral flow is negligible. This cross-sectionally homogeneous flow occurs because the cross-section of the model domain is designed to be very narrow with constant bathymetry. One of the ways to generate lateral flows in the model is to incorporate cross-channel variations in the bathymetry of the estuary (Li and O'Donnell, 1997; Valle-Levinson et al., 2000) . For instance a parabolic bathymetric profile, where width equals to $L_{C,y} = 3.5$ km and total depth $H = 12$ m, is suggested (Fig. 29)

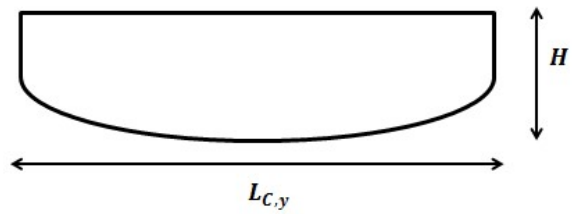

Figure 29: Suggested Bathymetric profile of the estuarine cross section. The width of the cross section is $L_{C,x}$ and the total depth is H.

An estuary with this bathymetric profile yields a situation where along-channel tidal currents are stronger at the deepest location of the estuarine cross-section and weaker at the sallowest locations. Because of this, lateral shear occurs at the along-channel currents. Consequently, advection of the along-channel density gradient results in a cross-channel density gradient. This yields a situation where, during the flood, density is larger in the deep part of the estuary compared to that in the shallow part. As a result, a lateral baroclinic pressure gradient is generated and drives lateral currents. Lerczak at Geyer (2004) pointed out that lateral circulation is oriented in such a direction that it supports the along-channel subtidal flow. It is clear that by considering a bathymetric profile with lateral variations in the model, the performed experiments will be more realistic and a better estimation about the generation of subtidal flow will be made.

5 Summary and Conclusions

This thesis focused on the coupled dynamics of water motion (turbulent mixing, tidal motion, subtidal flow) and salinity in estuaries. Seven numerical experiments were carried out using the Delft-3D model. The model domain considers the geometrical features of a real time basin (NP of Yangtze estuary). Freshwater discharge and tidal forcing (S_2 tide), which vary in each experiment, are specified at the head of the estuary and the seaward boundary, respectively. Firstly, a default experiment was conducted where tidal amplitude and river discharge were set $u_T \simeq 0.75\,\mathrm{ms}^{-1}$ and $Q = 2000\,\mathrm{m}^3\mathrm{s}^{-1}$, respectively. Subsequently, three experiments were conducted where the tidal amplitude had its default value and the river discharge increased from $Q = 1800\,\mathrm{m}^3\mathrm{s}^{-1}$ to $Q = 2400\,\mathrm{m}^3\mathrm{s}^{-1}$, and three more where river discharge had its default value and tidal amplitude increased from $u_T \simeq 0.68\,\mathrm{ms}^{-1}$ to $u_T \simeq 1.3\,\mathrm{ms}^{-1}$. The first specific aim of this thesis was to quantify and understand the variation of saltwater intrusion, stratification and turbulent mixing under varying tidal amplitude and river discharge. The second research question was to quantify and compare the contribution of different driving mechanisms (density gradient, river flow, asymmetric mixing) to total subtidal flow. Moreover, asymmetry in mixing during the tidal cycle leads to generation of subtidal flow due to covariance of eddy viscosity and vertical shear (CMS). By decomposing CMS, it was investigated either only covariance between

S_2 eddy viscosity and S_2 vertical shear (tidal straining) generates subtidal flow, or there is also contribution to subtidal flow from covariance between S_4 eddy viscosity and S_4 vertical shear.

Regarding saltwater intrusion L, which was defined here as the distance between the mouth of the estuary and the location where value of salinity at the bottom is $s_l = 2$ psu, it was found that it increases with tidal amplitude, while it decreases with river flow. Despite the fact that this was the expected behavior, the results are not in good agreement with those of a theoretical model by MacCready (2004). Furthermore, stratification at location $x = 45$ km in the estuary, which is expressed as top to bottom salinity difference Δs, was found to increase with river flow and decrease with tidal amplitude. The same pattern occurs also for the horizontal Richardson number Ri_x, which is computed at the location where tidally averaged depth-mean salinity is half of that at the mouth of the estuary, and it stands for another measure of stratification. Both values of Δs and Ri_x are underestimated and this is due to the fact that in the experiments a large and non-realistic horizontal diffusion coefficient was considered. Finally, the vertical profiles of residual, S_2 and S_4 eddy viscosity are computed and it is found that both their values of maximum mixing and mixing length increase with increasing tidal current amplitude. The observed increase of the mixing length with tidal current amplitude is consistent with the values of nondimensional bottom boundary layer where the latter were computed by a theoretical model of Stacey and Ralston (2005).

Total subtidal flow is decomposed into it's components due to different driving mechanisms, where the latter are computed from analytical expressions (Cheng et al., 2013). In particular, subtidal flow due to river discharge, density gradient and asymmetry in tidal mixing are computed for the default experiment ($Q = 2000\,\mathrm{m^3s^{-1}}$, $u_T \simeq 0.75\,\mathrm{ms^{-1}}$) and the experiment with the lowest tidal current amplitude ($Q = 2000\,\mathrm{m^3s^{-1}}$, $u_T \simeq 0.63\,\mathrm{ms^{-1}}$). Regarding the river-induced flow, it was found that it has the same magnitude and seaward direction in both experiments, but its vertical profile is logarithmic at the experiment with the lowest tidal current amplitude and linear at the default experiment. Density-driven flow is directed seawards at the upper part of the water column, while at the lower part it is directed landwards. It was found that subtidal flow due to density gradient is much stronger for the experiment with the lowest tidal current amplitude compared to the default experiment. Subtidal flow due to mixing asymmetries does not contribute significantly to total subtidal flow and it was found to have the opposite direction of the density-driven flow in both experiments. In the default experiment, the subtidal flow due to asymmetric mixing has the opposite structure of that of density-driven flow because larger mixing occurs during ebb than flood. In the experiment with the lowest tidal amplitude, the subtidal flow due to asymmetric turned out to be again inverse compared to the direction of density-driven flow. This result is consistent with the subtidal flow due to asymmetric mixing, found at Cheng et al. (2013) for stratified conditions. Finally from the CMS decomposition it was found that in the experiment with the lowest tidal amplitude only tidal straining, represented by the covariance between S_2 eddy viscosity and S_2 vertical shear, generates subtidal flow. On the contrary, in the default experiment it was found that covariance of S_4 eddy viscosity and S_4 vertical shear generates subtidal flow as well.

6 Appendix: Analytical expressions of along-estuary subtidal currents

River-induced flow

The solution for the river-induced flow is,

$$\overline{u_R} = gH^2 \frac{\partial \bar{\eta}_R}{\partial x} \int_{-1}^{\sigma} \frac{\sigma^{'}}{\bar{A}_v} d\sigma^{'} \tag{34}$$

with

$$\frac{\partial \bar{\eta}_R}{\partial x} = \frac{q}{gH^2 \int_{-1}^{0} \int_{-1}^{\sigma} \frac{\sigma^{'}}{\bar{A}_v} d\sigma^{'} d\sigma} \tag{35}$$

Density-driven flow

The solution for the density-driven flow is,

$$\overline{u_D} = gH^2 \frac{\partial \bar{\eta}_D}{\partial x} \int_{-1}^{\sigma} \frac{\sigma^{'}}{\bar{A}_v} d\sigma^{'} - \frac{gH^2}{\rho_0} \int_{-1}^{\sigma} \left\{ \frac{1}{\bar{A}_v} \int_{\sigma^{'}}^{0} \left[\int_{\sigma^{''}}^{0} \frac{\partial \overline{(H_C+\eta)\rho}}{\partial x} d\sigma^{'''} + \overline{\rho\sigma^{''} \frac{\partial (H_C+\eta)}{\partial x}} \right] d\sigma^{''} \right\} d\sigma^{'} \tag{36}$$

with

$$\frac{\partial \bar{\eta}_D}{\partial x} = \frac{\int_{-1}^{0} \int_{-1}^{\sigma} \left\{ \frac{1}{\bar{A}_v} \int_{\sigma^{'}}^{0} \left[\int_{\sigma^{''}}^{0} \frac{\partial \overline{(H_C+\eta)\rho}}{\partial x} d\sigma^{'''} + \overline{\rho\sigma^{''} \frac{\partial (H_C+\eta)}{\partial x}} \right] d\sigma^{''} \right\} d\sigma^{'} d\sigma}{\rho_0 \int_{-1}^{0} \int_{-1}^{\sigma} \frac{\sigma^{'}}{\bar{A}_v} d\sigma^{'} d\sigma} \tag{37}$$

Advection-induced flow

The solution for the advection-induced flow is,

$$\overline{u_A} = gH^2 \frac{\partial \bar{\eta}_A}{\partial x} \int_{-1}^{\sigma} \frac{\sigma^{'}}{\bar{A}_v} d\sigma^{'} - H^2 \int_{-1}^{\sigma} \left[\frac{1}{\bar{A}_v} \int_{\sigma^{'}}^{0} \left(\overline{u \frac{\partial u}{\partial x}} + \overline{u \frac{\partial u}{\partial \sigma^{''}}} \right) d\sigma^{''} \right] d\sigma^{'} \tag{38}$$

with

$$\frac{\partial \bar{\eta}_A}{\partial x} = \frac{\int_{-1}^{0} \int_{-1}^{\sigma} \left[\frac{1}{\bar{A}_v} \int_{\sigma^{'}}^{0} \left(\overline{u \frac{\partial u}{\partial x}} + \overline{u \frac{\partial u}{\partial \sigma^{''}}} \right) d\sigma^{''} \right] d\sigma^{'} d\sigma}{g \int_{-1}^{0} \int_{-1}^{\sigma} \frac{\sigma^{'}}{\bar{A}_v} d\sigma^{'} d\sigma} \tag{39}$$

ATM-induced flow

The solution for the ATM-induced flow is,

$$\overline{u_{ATM}} = gH^2 \frac{\partial \bar{\eta}_T}{\partial x} \int_{-1}^{\sigma} \frac{\sigma^{'}}{\bar{A}_v} d\sigma^{'} - \int_{-1}^{\sigma} \frac{1}{\bar{A}_v} \overline{A_v^{'} \frac{\partial u^{'}}{\partial \sigma^{''}}} d\sigma^{'} +$$

$$+H^2 \int_{-1}^{\sigma} \left\{ \frac{1}{\bar{K_m}} \int_{\sigma^{'}}^{0} \left[\overline{\frac{2\eta}{H^3} \frac{\partial}{\partial \sigma^{''}} \left(A_v \frac{\partial u^{'}}{\partial \sigma^{''}} \right)} + \overline{\frac{2\eta}{H^3} \frac{\partial}{\partial \sigma^{''}} \left(A_v^{'} \frac{\partial \bar{u}}{\partial \sigma^{''}} \right)} + \overline{\frac{2\eta}{H^3} \frac{\partial}{\partial \sigma^{''}} \left(A_v^{'} \frac{\partial u^{'}}{\partial \sigma^{''}} \right)} \right] d\sigma^{''} \right\} d\sigma^{'} \tag{40}$$

with

$$\frac{\partial \bar{\eta}_{ATM}}{\partial x} = \frac{\int_{-1}^{0} \int_{-1}^{\sigma} \frac{1}{\bar{K_m}} \overline{A_v^{'} \frac{\partial u^{'}}{\partial \sigma^{'}}} d\sigma^{'} d\sigma}{gH^2 \int_{-1}^{0} \int_{-1}^{\sigma} \frac{\sigma^{'}}{\bar{A}_v} d\sigma^{'} d\sigma} -$$

$$- \frac{\int_{-1}^{0} \int_{-1}^{\sigma} \left\{ \frac{1}{\bar{A}_v} \int_{\sigma^{'}}^{0} \left[\overline{\frac{2\eta}{H^3} \frac{\partial}{\partial \sigma^{''}} \left(\bar{A}_v \frac{\partial u^{'}}{\partial \sigma^{''}} \right)} + \overline{\frac{2\eta}{H^3} \frac{\partial}{\partial \sigma^{''}} \left(A_v^{'} \frac{\partial \bar{u}}{\partial \sigma^{''}} \right)} + \overline{\frac{2\eta}{H^3} \frac{\partial}{\partial \sigma^{''}} \left(A_v^{'} \frac{\partial u^{'}}{\partial \sigma^{''}} \right)} \right] d\sigma^{''} \right\} d\sigma^{'} d\sigma}{g \int_{-1}^{0} \int_{-1}^{\sigma} \frac{\sigma^{'}}{\bar{A}_v} d\sigma^{'} d\sigma} \tag{41}$$

Stokes return flow

The solution for the Stokes return flow is,

$$\overline{u_S} = gH^2 \frac{\partial \bar{\eta}_S}{\partial x} \int_{-1}^{\sigma} \frac{\sigma^{'}}{\bar{A}_v} d\sigma^{'} \tag{42}$$

with

$$\frac{\partial \bar{\eta}_S}{\partial x} = \frac{-\int_{-1}^{0} \overline{\eta u^{'}} d\sigma}{gH^3 \int_{-1}^{0} \int_{-1}^{\sigma} \frac{\sigma^{'}}{\bar{A}_v} d\sigma^{'} d\sigma} \tag{43}$$

.

7 References

Burchard, H., and R. Hofmeister (2008), A dynamics equation for the potential energy anomaly for analyzing mixing and stratification in estuaries and coastal seas, *Estuar. Coast. Shelf S.*, 77, 679–687.

Chatwin , P. C. (1976), Some remarks on the maintenance of the salinity distribution in estuaries, *Estuar. Coast. Mar.* Sci., 4, 555-566.

Cheng, P., A. Valle-Levinson, and H. E, de Swart (2011), A numerical study of residual circulation induced by asymmetric tidal mixing in tidally dominated estuaries, *J. Geophys. Res., 116*, C01017, doi:10.1029/2010JC006137.

De Swart, H.E. (2012). Physics of coastal systems. Lecture notes, version 2012-2013. Utrecht University, The Netherlands. (Chapter 3)

Díez-Minguito, M., E. Contreras, M. J. Polo, and M. A. Losada (2013), Spatio-temporal distribution, along-channel transport, and post-riverflood recovery of salinity in the Guadalquivir estuary (SW Spain), *J. Geophys. Res. Oceans*, 118, 2267–2278, doi:10.1002/jgrc.20172.

Dyer, K. R., (1997): Estuaries: A Physical Introduction. 2d ed. John Wiley and Sons, 195 pp.

Hansen, D. V., and M. Rattray (1965), Gravitational circulation in straits and estuaries, *J. Mar. Res.*, 23, 104–122.

Ianniello, J. P. (1977), Tidally induced residual currents in estuaries of breadth and depth, *J. Mar. Res.*, 35, 755–786.

Jay, D. A., and J. D. Musiak (1994), Particle trapping in estuarine tidal flows, *J. Geophys. Res.*, 99, 445–461.

Jiang C, Li J, H. E. de Swart (2012), Effects of navigational works on morphological changes in the bar area of the Yangtze Estuary, *Geomorphology* 139–140:205–219.

Lerczak J. A. and W. R. Geyer (2004), Modeling the lateral circulation in straight, stratified Estuaries, *J. Phys. Oceanogr.*, 34, 1410–1428.

Li, C., and J. O'Donnell, Tidally driven residual circulation in shallow estuaries with lateral depth variation, *J. Geophys. Res.*, 102, 27,915-27,929, 1997

MacCready, P. (1999), Estuarine adjustment to changes in river flow and tidal mixing, *J. Phys. Oceanogr.*, 29(4), 708–726.

MacCready, P. (2004), Toward a unified theory of tidally-averaged estuarine salinity structure, *Estuaries,* 27(4), 561–570.

McCarthy, R. K. (1993), Residual currents in tidally dominated, well-mixed estuaries, Tellus A, 45(4), 325–340.

Monismith, S. G., W. Kimmerer, J. R. Burau, and M. T. Stacey (2002), Structure and flow-induced variability of the subtidal salinity field in Northern San Francisco Bay, *J. Phys. Oceanogr.*, 32, 3003– 3019.

Pritchard, D.W., (1952), Salinity distribution and circulation in the Chesapeake Bay estuarine system, *J. Mar. Res.* 11, 106–123.

Pritchard, D.W., (1954), A Study of the salt balance of a coastal plain estuary, *J. Mar. Res.* 13, 133–144.

Pritchard, D.W., (1956), The dynamic structure of a coastal plain estuary, *J. Mar. Res.* 15, 33–42.

Postma, H., Hydrography of the Dutch Wadden Sea, *Arch Neerl. Zool.*, 10, 405-511, 1961.

Ralston D. K., W. R. Geyer, and J. A. Lerczak (2008), Subtidal salinity and velocity in the Hudson River Estuary: Observations and Modeling, *J. Phys. Oceanogr.*, 38, 753–770.

Simpson, J. H., J. Brown, J. Matthews, and G. Allen (1990), Tidal straining, density currents, and stirring in the control of estuarine stratification, *Estuaries* 13(2), 125–132.

Stacey, M. T., and D. K. Ralston (2005), The scaling and structure of the estuarine bottom boundary layer, J. Phys. Oceanogr., 35(1), 55–71.

Talke S.A., H. E. de Swart, and H. M. Schuttelaars (2009), Feedback between residual circulation and sediment distribution in highly turbid estuaries: an analytical model, *Cont. Shelf. Res.* 29:119–135. doi:10.1016/j.csr.2007.09.002.

Valle-Levinson, A., C. Reyes, and R. Sanay, 2003: Effects of bathymetry, friction, and rotation on estuary–ocean exchange. J. Phys. Oceanogr., 33, 2375–2393.